ORNL/TM-6099

Analytical Investigation of Multicavity Prestressed Concrete Pressure Vessels for Elastic Loading Conditions

D. N. Fanning

OAK RIDGE NATIONAL LABORATORY
OPERATED BY UNION CARBIDE CORPORATION · FOR THE DEPARTMENT OF ENERGY

DISCLAIMER

Printed in the United States of America. Available from
National Technical Information Service
U.S. Department of Commerce
5285 Port Royal Road, Springfield, Virginia 22161
Price: Printed Copy ~~$6.00~~ 5.25 Microfiche $3.00

ORNL/TM-6099
Dist. Category UC-77

Contract No. W-7405-eng-26

Engineering Technology Division

HTGR BASE TECHNOLOGY PROGRAM

Prestressed Concrete Nuclear Pressure
Vessel Development (189a 01331)

Milestone No. 1c

ANALYTICAL INVESTIGATION OF MULTICAVITY PRESTRESSED CONCRETE PRESSURE VESSELS FOR ELASTIC LOADING CONDITIONS

D. N. Fanning

Date Published - September 1978

Prepared by the
OAK RIDGE NATIONAL LABORATORY
Oak Ridge, Tennessee 37830
operated by
UNION CARBIDE CORPORATION
for the
DEPARTMENT OF ENERGY

THIS PAGE

WAS INTENTIONALLY

LEFT BLANK

CONTENTS

ANALYTICAL INVESTIGATION OF MULTICAVITY PRESTRESSED CONCRETE PRESSURE VESSELS FOR ELASTIC LOADING CONDITIONS

D. N. Fanning

ABSTRACT

A three-dimensional finite-element analysis of a commercial high-temperature gas-cooled reactor (HTGR) was made using the finite-element code STATIC-SAP. Four loading conditions were analyzed elastically to evaluate the behavior of the concentric core prestressed concrete reactor vessel (PCRV) of the HTGR. The results of the analysis were evaluated in accordance with Section III, Division 2, of the ASME Code for Reactor Vessels and Containments. The calculated maximum stresses were found to be well within the Code-allowable values. The analysis was preceded by an evaluation of candidate computer codes using comparisons of experimental data with analytical results for the Ohbayashi-Gumi multicavity PCRV model. This vessel was chosen as a basis for comparison because of its geometrical similarity to the large multicavity PCRV and the anticipated availability of a complete set of the original experimental data. Although we were unable to obtain the original data, sufficient data were available in the open literature to permit limited but meaningful comparisons to be made. The three-dimensional finite-element codes NONSAP and STATIC-SAP were used for the analysis of the Ohbayashi-Gumi vessel.

INTRODUCTION

The objective of this study was to use elastic analysis to investigate the behavior of a concentric core prestressed concrete reactor vessel (PCRV) representative of a current-generation multicavity vessel. The primary concern was to identify areas where the stress in the vessel exceeds the stress allowed by the ASME Code for Reactor Vessels and Containments. The PCRV studied is for a 2000-MW(t) HTGR designed by General Atomic (GA). The PCRV has a central core cavity; four steam-generator cavities and two auxiliary circulator cavities are situated in the wall of the vessel.

The HTGR was analyzed using the three-dimensional finite-element computer code STATIC-SAP.[1] Prior to the analysis of the HTGR, a series of analyses was made to provide a measure of verification of the finite-element computer codes utilized. The model used for the verification

analyses was the Ohbayashi-Gumi multicavity PCRV. This vessel was chosen because of its geometric similarity to the HTGR and because the test data were thought to be easily obtainable. Although the original experimental data could not be obtained, sufficient data were available in the open literature[2] to permit limited comparisons.

THE OHBAYASHI-GUMI TEST VESSEL

Description

The Ohbayashi-Gumi multicavity test vessel, shown in Figs. 1 and 2, is a 1/20-scale model of a 1000-MW(e) HTGR. It has six steam-generator cavities arranged symmetrically about the central cavity as shown in Sections A and C of Figs. 1 and 2. A starlike concrete support structure (Section D) was connected rigidly beneath the bottom slab. The concrete had an ultimate strength of 44.6 MPa (6500 psi), and a 2.3-mm-thick (0.09-in.) liner served as the pressure boundary. Vertical prestressing was applied by 60 axial tendons, and circumferential prestressing was applied by winding wire under tension around the outside of the vessel, which was instrumented with embedded-type gages for measuring concrete strains.

Analysis

The first analytical model of the Ohbayashi-Gumi vessel was generated using 20-node elements. This type of element was selected because it is economical and offers advantages in modeling curved boundaries such as the vessel outer wall. Since the edges of the 20-node element are described quadratically, a smaller number of elements is required to represent curved surfaces than the number required when linear elements are employed. The in-core solution routine of NONSAP[3] severely limits the number of elements which can be used, thus forcing the omission of the steel closures and bearing pads. Figure 3 shows the resulting analytical model. Curved edges of the elements are represented in the figure by two straight lines. The model consists of a 30° sector of the vessel region above midheight of the reactor cavity. The midheight

symmetry assumed for this model represents an approximation of the actual vessel since the bottom head of the actual vessel is one-third thicker than the top head and is further stiffened by the support structure.

Comparisons between the analytical results and the experimental data are made for three loads: (1) vertical prestressing, (2) circumferential prestressing, and (3) operating pressure of 4.9 MPa (711 psi). The comparisons are for the vertical cross section midway between the steam-generator cavities (left half of Section I of Fig. 1). In the figures, the positive signs signify tension and negative signs signify compression. The calculated axial strains due to vertical prestressing are slightly larger than the corresponding experimental values (see Fig. 4), a discrepancy which apparently is due to the use of too small a modulus of elasticity or too large a value of prestressing for the analytical calculations.

The calculated radial strains due to the circumferential prestress show good agreement with the experimental data as seen in Fig. 5. The hoop strains produced by the circumferential prestressing are presented in Fig. 6. This analysis agrees fairly well with the experimental results except in the wall of the vessel near the reactor cavity, where the analytical results are approximately double the experimental results. The correctness of the experimental data is questionable, however, since the hoop strains measured in the walls between steam-generator cavities are larger than those in the wall sections where the concrete is continuous in the hoop direction. The radial strains due to internal pressure are presented in Fig. 7. The agreement between the experimental values and the analytical values is reasonable. The comparison between the experimental and analytical values for hoop strain due to pressure is poor (see Fig. 8). In general, the analytical values are about 50 μm/m more tensile than the experimental values. Unfortunately, the gages are not located in the regions of highest strain.

In an attempt to assess the magnitude of error introduced by failure to model the steel closures and bearing pads, a second analytical model was generated which includes these features. As with the first model, only the portion of the vessel above the midheight of the reactor cavity

was modeled (see Fig. 9). The greater geometric detail of this model, compared with that of the first, prevented the use of 20-node elements. Instead, 8-node elements were used to model most of the vessel, and midside nodes were added where the geometry required curved edges. The use of the lower order elements was dictated by limitations imposed by the NONSAP in-core solution routine. Results of the second analysis are presented in Figs. 10 through 14.

In Fig. 10 the contour lines showing calculated axial strains due to vertical prestressing differ appreciably from those of the first analysis (Fig. 4). This is particularly evident in the top slab region and at the haunch. However, there is little difference between the results for the two analyses in the instrumented region of the vessel wall.

In the case of the radial strains due to circumferential prestress, model 1 (Fig. 5) exhibited a much higher concentration at the haunch than model 2 (Fig. 11), a difference which can be explained by characteristics of the elements employed in the two analytical models. The higher order 20-node element used for the first analysis is more capable of identifying regions subjected to steep strain gradients than the 8-node element used for the second analysis.

The contour lines for hoop strain due to circumferential prestressing, shown in Fig. 12 for the second analysis, are essentially identical to those of the first model (Fig. 6). The same differences in stress concentrations that were previously discussed with respect to the radial strains resulting from circumferential prestress can be seen when comparing the radial strains due to internal pressure for the first (Fig. 7) and second (Fig. 13) analyses; however, the values in the instrumented region of the vessel for the two analyses are virtually the same. In both analyses, the central portion of the top slab has a tensile radial strain; but, whereas Fig. 7 shows a linear variation in strain through the thickness of the slab, Fig. 13 indicates a constant strain. This is probably related to the fact that 20-node elements used in model 1 can accommodate linear strains, while the 8-node elements of model 2 can only have constant strains on any given edge. The only case where model 2 appears to be clearly superior to model 1 is in that of the hoop strain due to pressure. The results for model 2 (Fig. 14) show a compressive

hoop strain in the wall of the vessel between steam-generator cavities as do the experimental data, but model 1 results (Fig. 8) show no compressive strains in this region.

The results of the Ohbayashi-Gumi multicavity PCRV model analytical studies conducted thus far using NONSAP have indicated that the geometric representations used in the analytical model were too crude to accurately represent the actual physical model. Consequently, the three-dimensional finite-element code STATIC-SAP was used to conduct a final analysis of the Ohbayashi-Gumi model prior to analyzing the proposed multicavity PCRV design for a commercial HTGR. STATIC-SAP has an out-of-core solution routine which enables it to accommodate a much larger problem than NONSAP.

The finite-element model of the Ohbayashi-Gumi vessel developed for use with STATIC-SAP is shown in Fig. 15. It represents a 30° sector of the vessel as did the previous models, but it also models the full height of the vessel, thereby eliminating the previous assumption of midheight symmetry. Twenty-node elements are used throughout the model except for the two layers of elements designated by the cross-hatching in Fig. 15. Sixteen-node elements are used in these regions to significantly reduce the bandwidth of the structural stiffness matrix. The bearing pads for the vertical prestressing cables, the steel plate pressure boundaries above the steam-generator cavities, and the support structure were included in the analytical model.

The contour lines in Fig. 16 showing calculated axial strains due to vertical prestressing are essentially identical to those of the second analysis (Fig. 10), which indicates that it is not necessary to use the higher order elements for this loading condition. This conclusion is not surprising since the vertical prestress does not cause appreciable bending. A comparison of the axial prestressing strains for the last two models with the first shows the importance of modeling the bearing pads for the vertical prestressing tendons for accurate results in the region of the top slab near the prestressing tendons.

The radial strains resulting from circumferential prestress, Fig. 17, show tension along the inner surface of the vessel wall as in Fig. 5 for model 1. As mentioned previously, the use of lower order elements

in the second model is probably the reason why the tensile zone of Fig. 11 does not extend to the haunch. To accurately calculate the radial strains due to this loading, it appears to be necessary to use the higher order elements. The hoop strains due to circumferential prestressing shown in Fig. 18 are almost identical to those presented in Figs. 6 and 12.

The hoop strains due to internal pressure shown in Fig. 19, like those for model 2 (Fig. 14), agree well with the experimental data. Figure 19 also shows a linear variation in strain through the thickness of the central portion of the top slab similar to the analytical results of model 1 (Fig. 8).

Because the experimental data were restricted to regions where the strains varied relatively slowly, the evaluation of the relative merits of the three models had to be made with little regard for the actual experimental and analytical comparisons; fortunately, the results of all the models were reasonable and essentially the same in the instrumented region of the vessel. However, by looking at other regions of the vessel, such as the area under the vertical prestressing bearing pads, it was apparent that model 1 lacked sufficient geometric detail. Also, the radial strains along the inner surface of the vessel wall indicated that the lower order elements of model 2 could not give a good representation of the complete vessel behavior. Some of the results of model 3 showed a distinct lack of symmetrical behavior above and below midheight of the reactor cavity. For the above reasons we elected to model the full height of the vessel using the more desirable 20-node elements for the subsequent analytical studies of a concentric core multicavity PCRV.

ANALYSIS OF HTGR

The analytical model of the concentric core PCRV is shown in Fig. 20. A 30° segment of the vessel is modeled using 213 20-node elements and 1667 nodes. The wall of the PCRV for the HTGR contains six cavities, four for steam generators and two for auxiliary circulators (Fig. 21). Since the vessel has two planes of symmetry, an accurate geometric model would consist of a 90° segment of the vessel; however,

the error introduced by modeling only 30° should be very small. Although the refueling penetrations in the top slab are not geometrically represented in the analytical model, their effect has been partially accounted for by modifying the material properties of the elements in this region. Five load cases were analyzed: (1) vertical prestressing, (2) circumferential prestressing, (3) pressure, (4) dead load, and (5) thermal load. The actual loading conditions were simulated by superposing the results of these five loads.

Thirty-one vertical tendons act upon the 30° segment of the vessel modeled; eight of these pass through the bottom head into the support structure, where they are anchored, and the others are anchored on the lower surface of the bottom head. The bearing pads associated with these tendons were too small to model without drastically increasing the size of the analytical model and the cost of the analysis. Although the analyses of the Ohbayashi-Gumi vessel indicated that the bearing pads should be included for accurate results in the top slab, we felt that the error introduced by omitting these pads on the HTGR would be insignificant because of the relatively large number of tendons, a condition which makes the vertical prestressing load more like a uniform pressure than the six tendons of the Ohbayashi-Gumi vessel. A preprocessor was used to convert the tendon forces into equivalent nodal loads.

The circumferential prestressing is arranged in 24 bands, each having 12 to 14 layers of 7-wire 12.7-mm-diam (0.5-in.) strands. Layers within each band alternate having 53 and 54 strands. The five bands around the top slab have an average tension of 96.3 MN (21,650 kips), which is equivalent to a pressure of 6.02 MPa (874 psi) on the outer wall of the vessel. Twelve bands compress the wall of the vessel between the top and bottom heads and exert the equivalent of 4.84 MPa (702 psi). The remaining seven bands around the bottom head are equivalent to a pressure of 5.73 MPa (831 psi) on the outside of the vessel. A preprocessor converted the pressure loadings into equivalent nodal loads for input to STATIC-SAP.

The pressure loading used for the analysis was the maximum cavity pressure (MCP) of 5.35 MPa (776 psi) instead of the operating pressure of 4.90 MPa (710 psi). This pressure was applied to the inside surfaces

of the reactor and steam-generator cavities and the crossover ducts. The upward thrust resulting from pressure on the steam-generator closure plug was simulated by an upward ring load on the top slab around the steam-generator penetration. As with the pressures on the outer wall which simulate the circumferential prestress, equivalent nodal loads were calculated by a preprocessor for the internal pressure loading.

The dead load consisted of several parts. The rebars, vertical prestressing tendons, tendon tubes, and load cells were considered to be uniformly distributed in the concrete, resulting in a weight density of 24.55 kN/m^3 (156 lb/ft^3) for the mixture. Eighty-five percent of the dead loads were included in the above mixture of concrete, steel, etc.; the weight of the circumferential tendons, steel channel liners, and associated load cells was included as a downward surface traction on the outer wall of the vessel. The weight of the control-rod drive assembly and the top deck was represented as a pressure on the top head. The steam-generator weight was distributed as a downward surface traction on the walls of the steam-generator cavity. The steam-generator closure plug weight was applied as a ring load on the top slab around the rim of the steam-generator cavity. The weight of the reactor core, the core support floor, and the segmented core barrel was applied to the bottom of the reactor cavity, and the weight of the liners and cooling tubes was neglected.

Nodal temperatures are required for the effect of the thermal load to be analyzed. A thermal diffusion analysis of a PCRV reported by Saugy et al.[4] was used to approximate the temperature distribution within the PCRV of the HTGR under analysis. The PCRV analyzed by Saugy was for a 1000-MW(e) gas-cooled fast reactor developed by the Swiss Federal Institute for Reactor Research. The Swiss PCRV differs from the one that we analyzed in that it has nine cavities in the vessel wall, whereas the latter has six. Another discrepancy is the 30 K (54°F) thermal gradient between the reactor cavity walls of the Swiss vessel and the external walls compared with the 39 K (70°F) thermal gradient of the HTGR vessel. A preprocessor program was written and used to calculate the temperatures at the nodes of the HTGR vessel using the thermal profiles for the Swiss PCRV. The resulting isotherms for a horizontal

section at midheight of the reactor cavity and for a vertical section through the steam-generator cavity are shown in Figs. 22 and 23. Two analyses of the thermal gradient loading condition were reported by Saugy. One analysis assumed that the temperature within any one finite element was constant and naturally resulted in a discontinuous thermal gradient within the vessel. Another analysis included the gradient within an element, thereby resulting in a more accurate continuous thermal gradient. Since the maximum stresses calculated using both assumptions were approximately the same and since STATIC-SAP uses a continuous thermal gradient representation, any errors introduced by using the temperature approximated from the report by Saugy (and shown in Figs. 22 and 23) should be insignificant.

COMPARISON OF ANALYTICAL RESULTS OF HTGR WITH OHBAYASHI-GUMI VESSEL

Although the modulus of elasticity for the HTGR is not the same as that for the Ohbayashi-Gumi multicavity vessel, 34.5 vs 31.0 GPa (5×10^6 vs 4.5×10^6 psi), they are sufficiently close to allow a reasonable comparison of strains and, of course, have no effect on the stresses. Poisson's ratio for the HTGR concrete is 0.17 while for the Ohbayashi-Gumi vessel it is 0.167, an insignificant difference.

The axial strains resulting from the vertical prestress shown in Fig. 24 are practically identical to those for the Ohbayashi-Gumi vessel (Fig. 16). Both vessels exhibit a high gradient in the top slab because of the concentrated prestressing forces. Both vessels also have tensile strains in the central portion of the top slab and high strain gradients at the haunches, and the walls of the vessels have almost constant strain through the thickness. The slightly higher strains in the wall of the Ohbayashi-Gumi vessel can be explained by its lower modulus of elasticity compared with that of the HTGR and its higher effective prestressing level.

The radial strains due to circumferential prestressing presented in Fig. 25 are very similar to the strains in the Ohbayashi-Gumi vessel for the same loading (Fig. 17). The inside surfaces of the walls of the

vessels have tensile strains of approximately 50 μm/m. The largest compressive strains, 300 μm/m, occur at the haunches of the vessels. The higher relative circumferential prestressing level of the HTGR probably causes the larger compressive strains in the top and bottom slabs of that vessel.

The hoop strains resulting from circumferential prestress (shown in Fig. 26) differ from those of the Ohbayashi-Gumi vessel (Fig. 18) primarily in the region of the vessel wall near the reactor cavity where the strains in the HTGR are approximately 80 μm/m more compressive. The different relative prestressing levels, as mentioned previously, are probably the major contributor to the larger strains in the HTGR. Throughout the remainder of the cross section, the strains in the two vessels are almost the same.

The hoop strains due to internal pressure, shown in Fig. 27, are very close (within 50 μm/m) to those for the Ohbayashi-Gumi vessel (Fig. 19). For both vessels the strains are most tensile along the wall of the reactor cavity near its midheight and compressive in the region of the vessel wall between steam-generator cavities.

The analytical results for the HTGR vessel appear to be reasonable based upon the comparisons that have been made with the earlier calculations for the Ohbayashi-Gumi model with a similar geometry. These results will be compared with the maximum allowable stresses prescribed by Section III, Division 2 of the ASME Code.[5]

EVALUATION OF HTGR

The following loading conditions were evaluated: (1) dead load plus prestressing; (2) dead load, prestressing with end-of-life losses, and temperature; (3) dead load, prestressing with end-of-life losses, and pressure; and (4) dead load with end-of-life losses, pressure, and temperature. The end-of-life prestress losses as obtained from the Delmarva Power and Light PSAR are 18 and 20% for the vertical and the circumferential prestress, respectively. For the analysis of the temperature loading, the modulus of elasticity was reduced by 50% as allowed in subparagraph CB-3310 (b) of the ASME Code. The 50% reduction is intended to

provide a conservative estimate of the reduction in stress resulting from creep.

The results for load condition 1, which represents the loads on the vessel immediately after the vessel has been prestressed, are presented in Figs. 28 through 33. According to Table CB-3421-1 of the ASME Code, the compressive stresses for this loading should not exceed $0.50f'_c$, which is 22.4 MPa (3250 psi) for the concrete of the HTGR; the tensile stresses should not exceed $6\sqrt{f'_c}$, which is 3.34 MPa (484 psi) for the concrete of this vessel. The stresses shown in Figs. 28 through 32 are all within the allowable limits; however, the allowable compressive stress is exceeded slightly in the ligament between the reactor cavity and the steam-generator cavity on the inside surface of the steam-generator cavity (Fig. 33). The volume of concrete that is overstressed is insignificant.

Results of load condition 2 are shown in Figs. 34 through 39. Since this loading includes secondary stresses caused by temperature, the allowable compressive stress is $0.6f'_c$, which is 26.9 MPa (3900 psi), and the allowable tensile stress is $7.5\sqrt{f'_c}$, which is 4.17 MPa (605 psi). The largest tensile stresses occur in the ligament between the reactor cavity and the steam-generator cavity near the crossover ducts (Fig. 36). The stress in these regions is approximately 2.76 MPa (400 psi), which is much lower than the 4.17-MPa (605-psi) maximum allowable tensile stress. The largest compressive stresses occurred in the same regions as the largest tensile stresses for this loading condition (Fig. 39). The 24.1-MPa (3500-psi) compressive stress that exists in the ligament does not exceed the 26.9-MPa (3900-psi) maximum allowable value.

Results for load condition 3 are presented in Figs. 40 through 45. The maximum allowable compressive stress for this loading is $0.45f'_c$, which is 20.2 MPa (2925 psi), and the limit for tensile stress is $6\sqrt{f'_c}$ [3.34 MPa (484 psi)]. The only tensile stresses for this loading occur at the upper haunch (Fig. 41) and at the top of the steam-generator cavity (Fig. 42). The tensile stresses at the upper haunch are very low, that is, less than 1.38 MPa (200 psi); however, the tensile stresses around the top of the steam-generator cavity are in excess of 6.9 MPa (1000 psi), which is considerably larger than the allowable value. These large tensile stresses are misleading because they are due primarily to the method

of modeling the effect of the pressure on the steam-generator cavity closure plug. In the analytical model, the pressure on the closure plug was represented by an upward ring load on the top head around the rim of the steam-generator cavity; in the actual vessel the load on the closure plug would be transferred to prestressing tendons rather than directly to the concrete. The net result is that the severe stress concentration in the analytical model does not accurately represent the conditions of the actual vessel in this localized region and the high stresses are therefore fictitious. This lack of similitude between the analytical model and the actual vessel also caused a concentration of compressive stresses at the top of the steam-generator cavity (Fig. 45). Except for this region, the compressive stresses are generally less than 6.9 MPa (1000 psi). All compressive stresses are less than the Code-allowable value of 20.2 MPa (2925 psi).

The results of load condition 4, which is essentially the normal operating condition [except the pressure is MCP instead of normal working pressure (NWP)], are presented in Figs. 46 through 51. For this loading the allowable compressive stress limit is $0.60f'_c$ [26.9 MPa (3900 psi)]; the tensile stress limit is $7.5\sqrt{f'_c}$ [4.17 MPa (605 psi)]. Except for the region around the top of the steam-generator cavity, the largest tensile stresses appear at the outer wall of the vessel at midheight (Figs. 46 through 48) and at the upper surface of the top head near the centerline of the vessel (Figs. 47 and 48). Stresses in these two regions are approximately 2.78 MPa (400 psi), which is within the Code-allowable limit. The large tensile stresses calculated for the region at the top of the steam-generator cavity are fictitious, as explained in the discussion of load condition 3. The compressive stresses are generally less than 6.9 MPa (1000 psi). The lack of similitude for the closure plug hold-down also results in a calculated concentration around the top of the steam-generator cavity; however, even the 12.4-MPa (1800-psi) compressive stress reached in this area is much less than the allowable limit.

CONCLUSION

According to the results of the elastic analysis, the HTGR vessel appears to be within the Code-allowable range for concrete stresses. The only region where the analysis indicated stresses exceeding the allowable limit is in the region around the top of the steam-generator cavity immediately below the steam-generator cavity closure plug attachment. The large tensile stresses calculated in this region of the vessel for load conditions which included internal pressure resulted from a lack of similitude between the actual closure plug hold-down and the method used for modeling the hold-down. The loading imposed on the analytical model resulted in a sizable stress concentration which does not exist in the actual model.

Compressive stresses exceed the Code-allowable values for point stress in a very small region of the ligament between the reactor cavity and the steam-generator cavity. However, all compressive forces can be resisted by the compression sectional area remaining when the concrete subjected to point stresses above those allowed is neglected as in paragraph CB-3440 of the ASME Code.

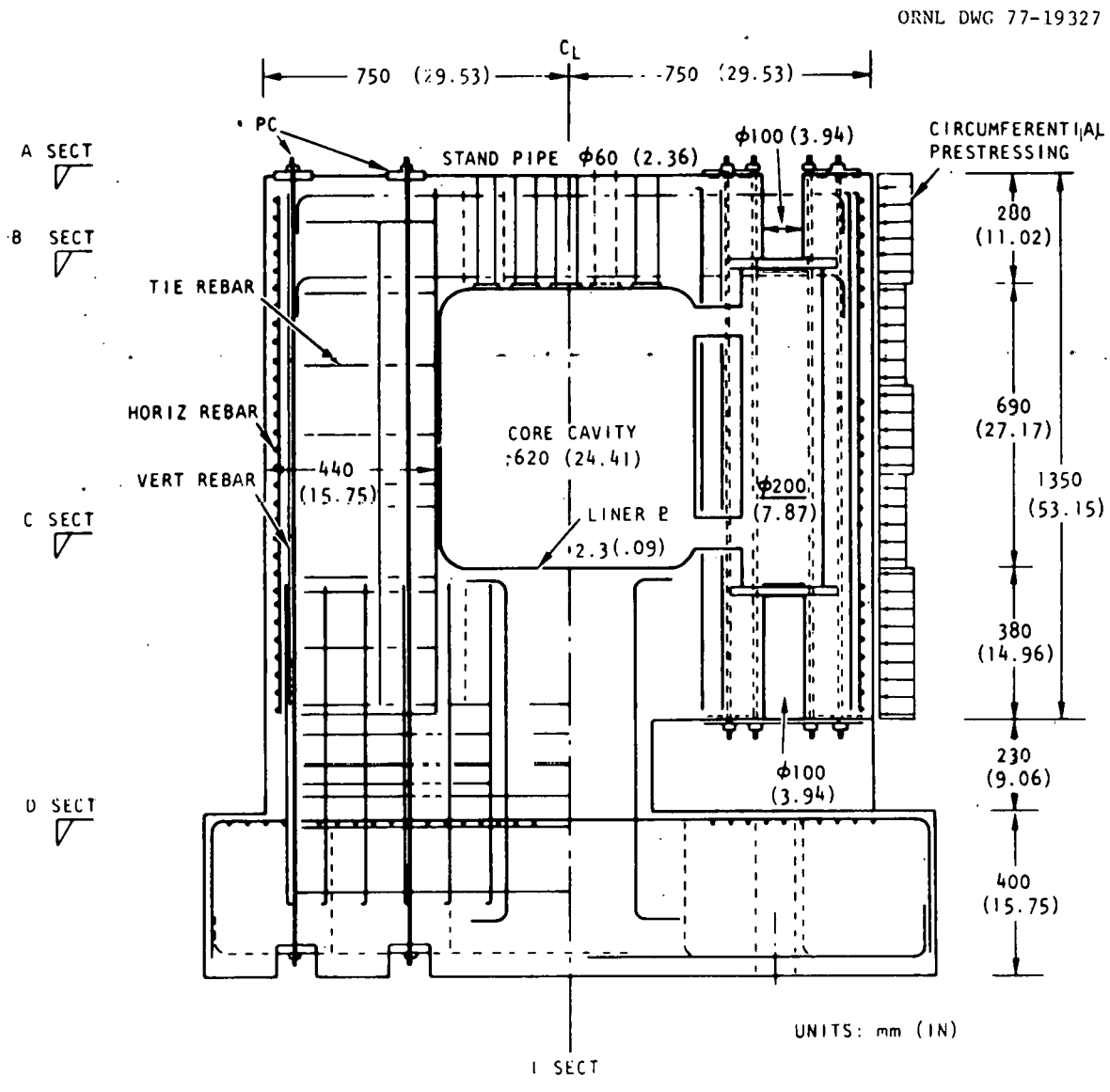

Fig. 1. General arrangement of Ohbayashi-Gumi vessel.

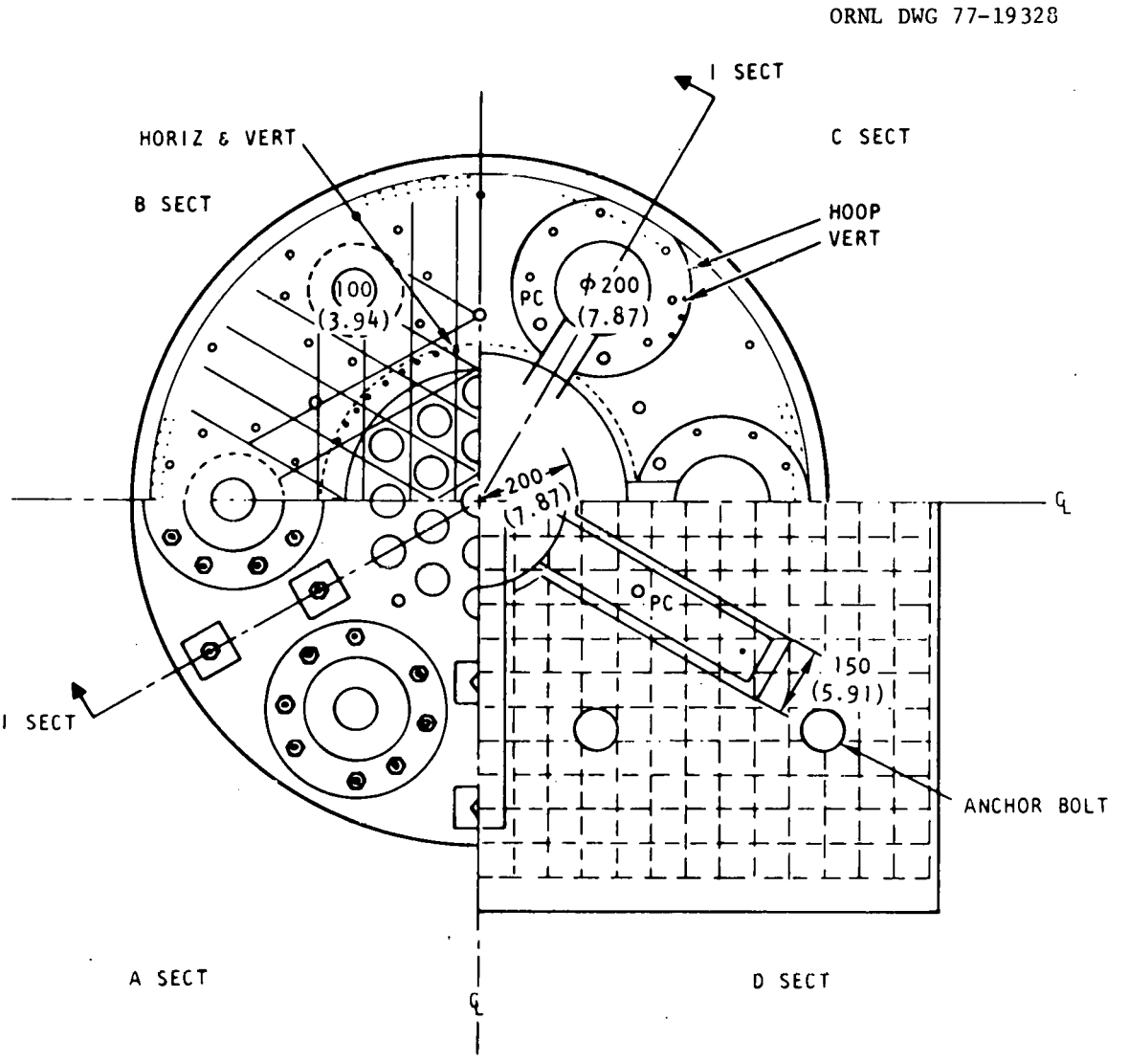

Fig. 2. Horizontal cross sections of Ohbayashi-Gumi vessel.

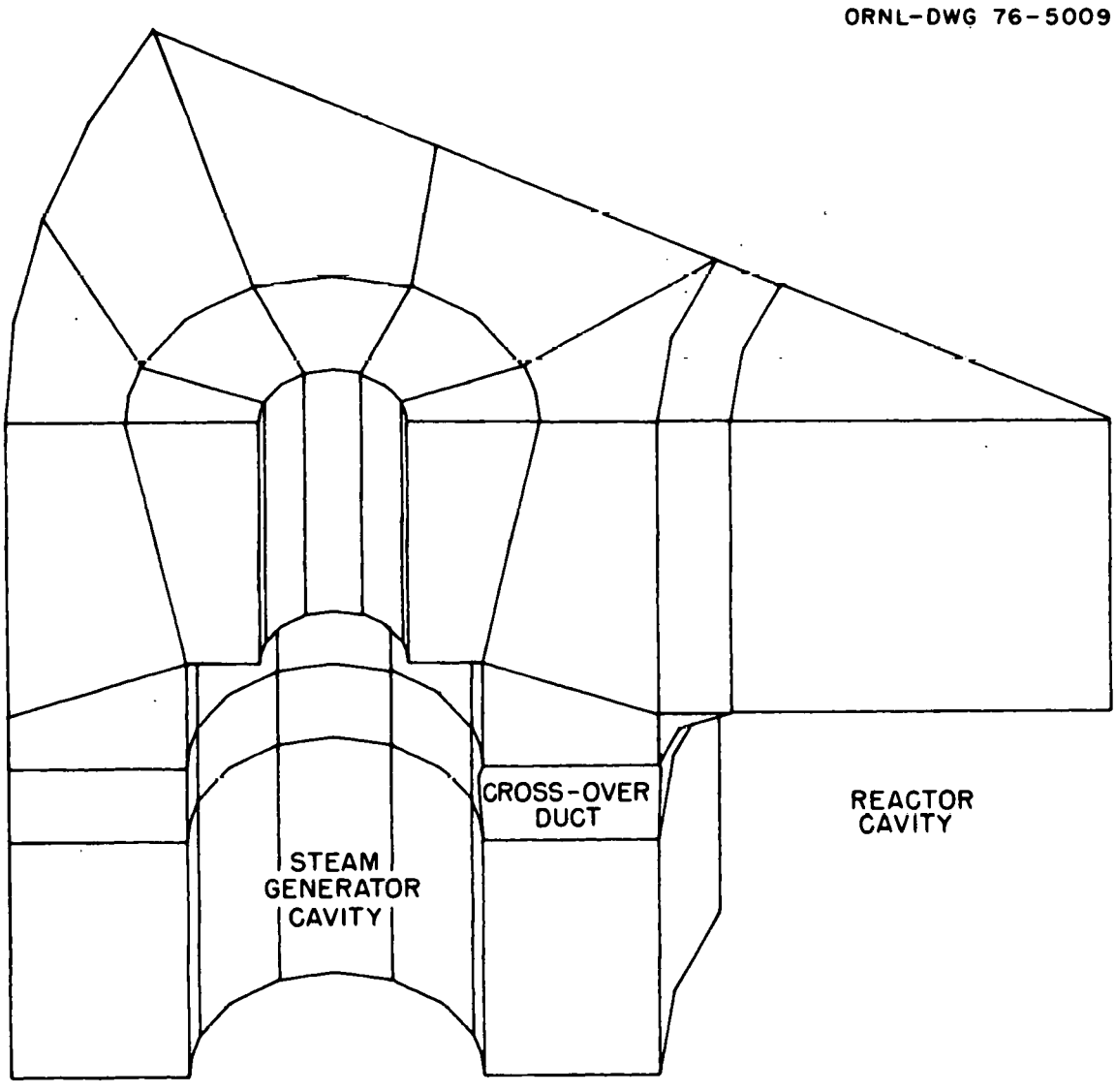

Fig. 3. Analytical model 1 of the Ohbayashi-Gumi vessel.

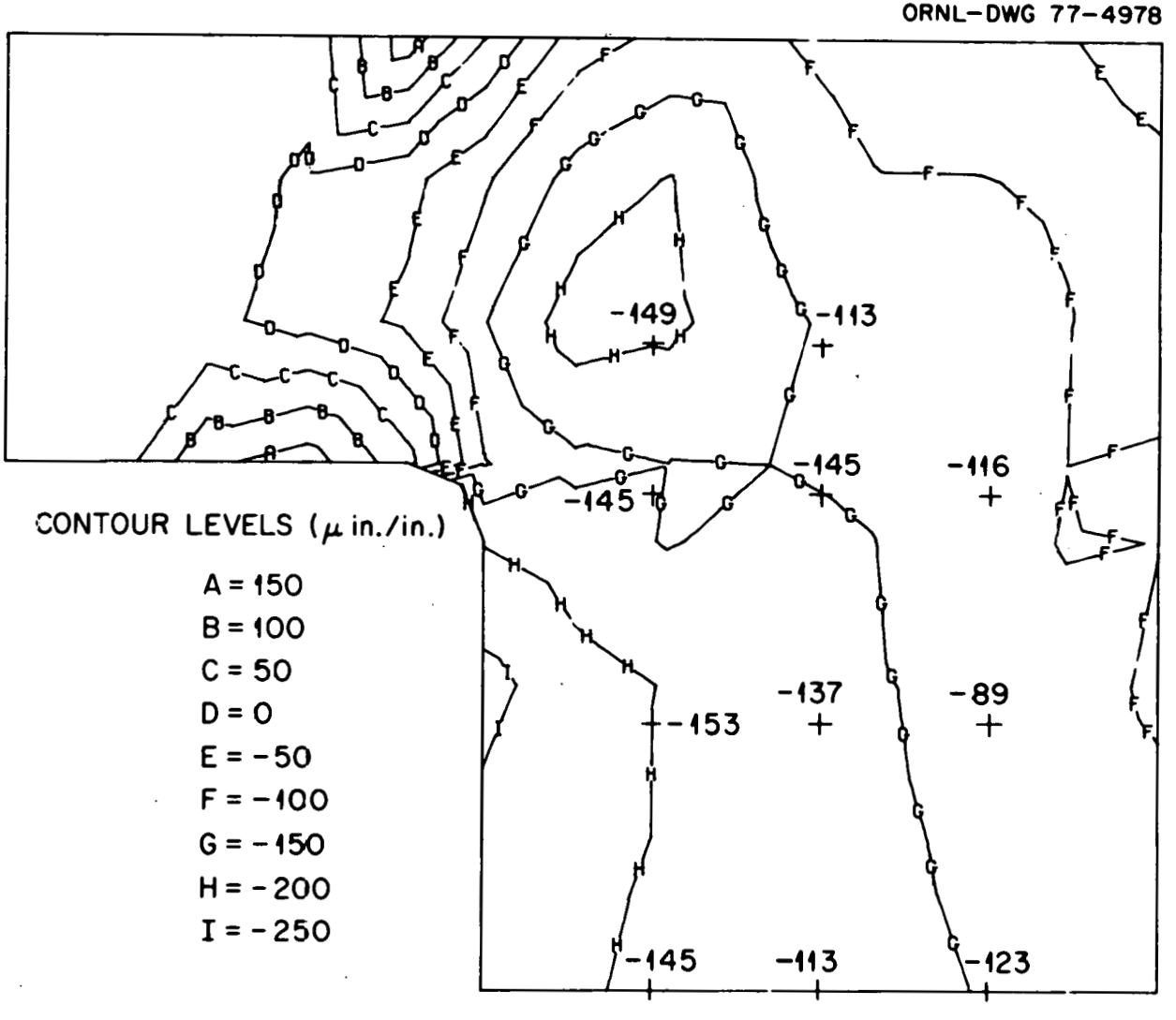

Fig. 4. Axial strains due to vertical prestressing for Ohbayashi-Gumi model 1. (Contours represent calculated values and points represent experimental values in millionths.)

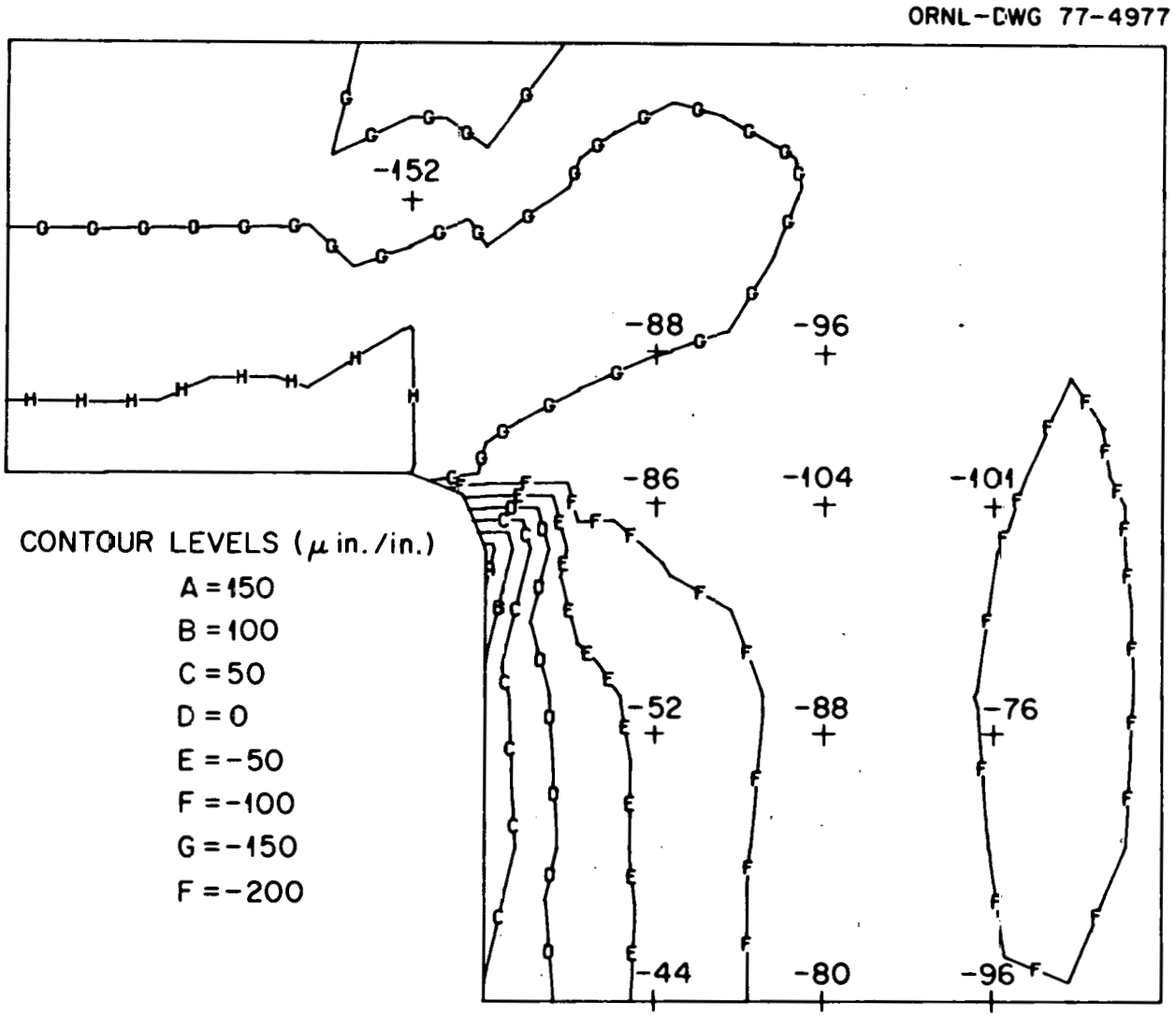

Fig. 5. Radial strains due to circumferential prestressing for Ohbayashi-Gumi model 1. (Contours represent calculated values and points represent experimental values in millionths.)

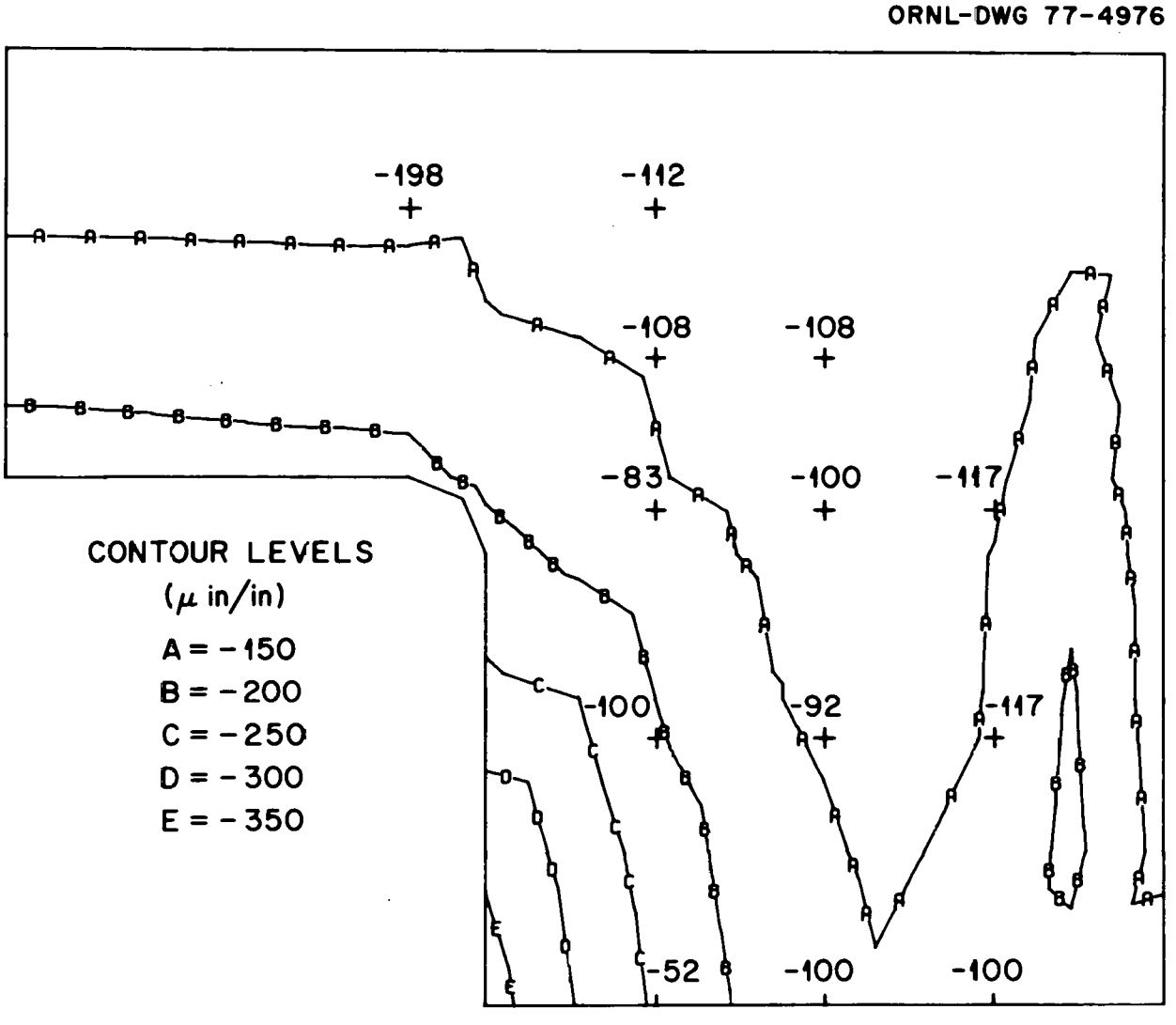

Fig. 6. Hoop strains due to circumferential prestressing for Ohbayashi-Gumi model 1. (Contours represent calculated values and points represent experimental values in millionths.)

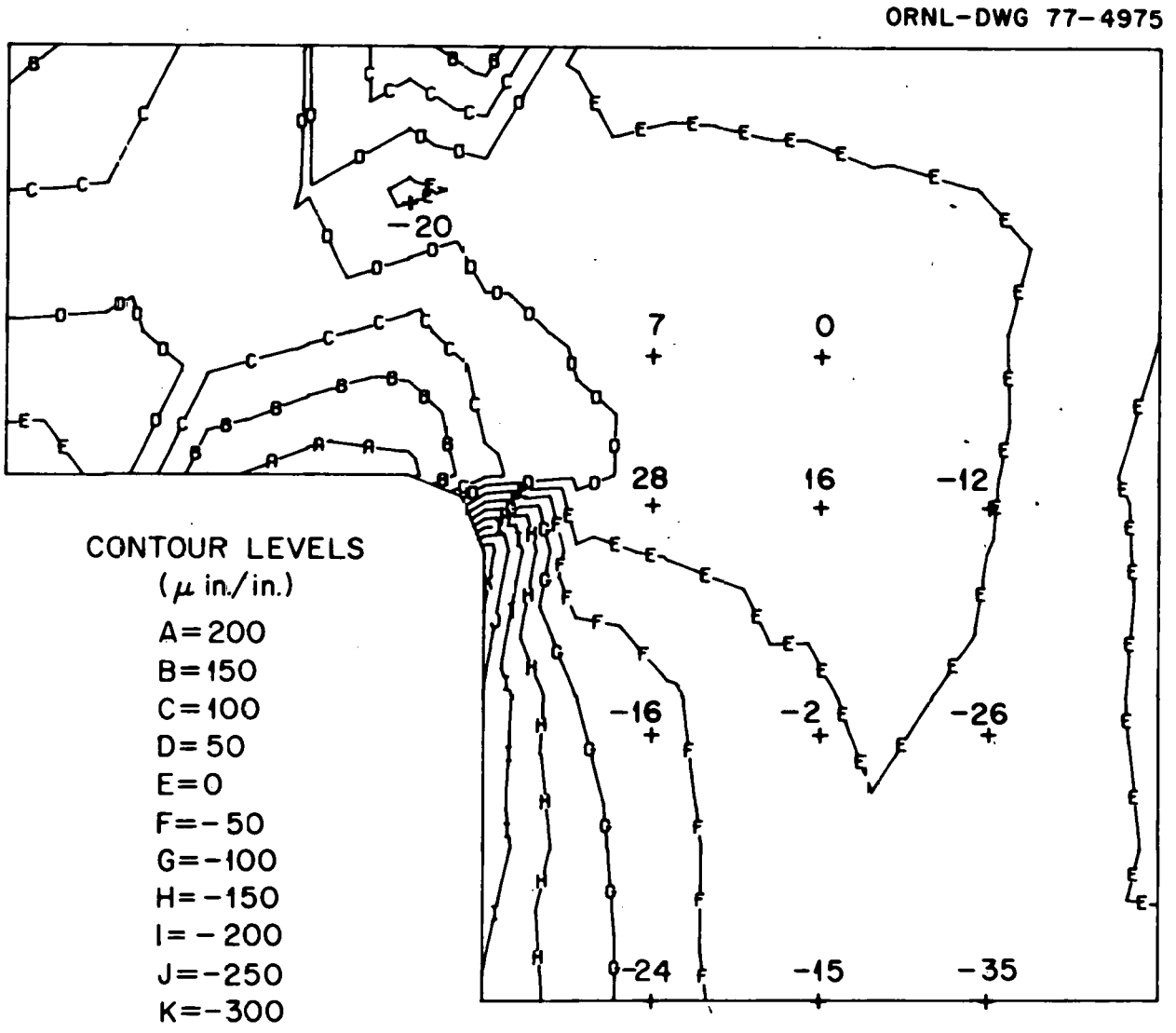

Fig. 7. Radial strains due to design pressure for Ohbayashi-Gumi model 1. (Contours represent calculated values and points represent experimental values in millionths.)

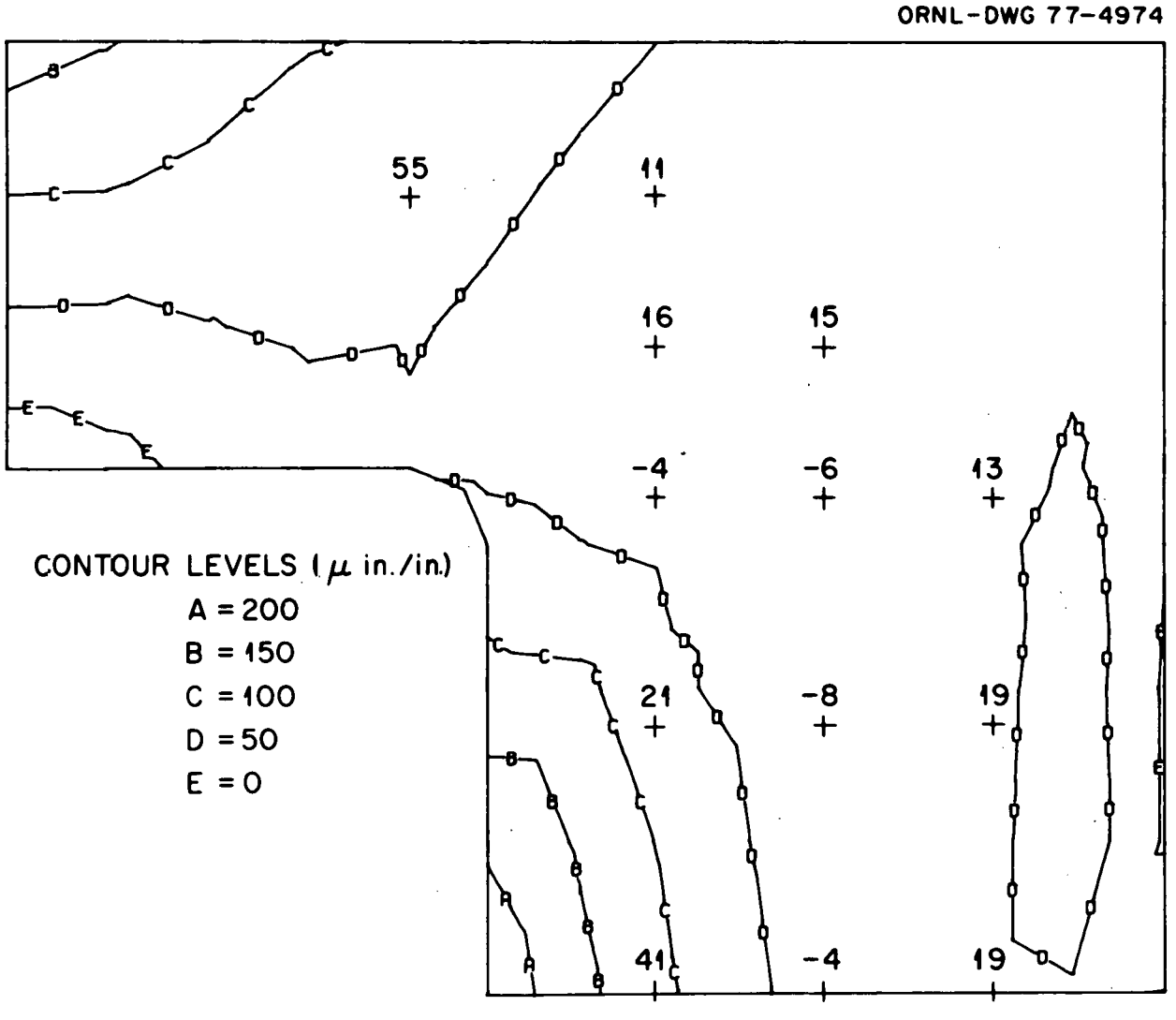

Fig. 8. Hoop strains due to design pressure for Ohbayashi-Gumi model 1. (Contours represent calculated values and points represent experimental values in millionths.)

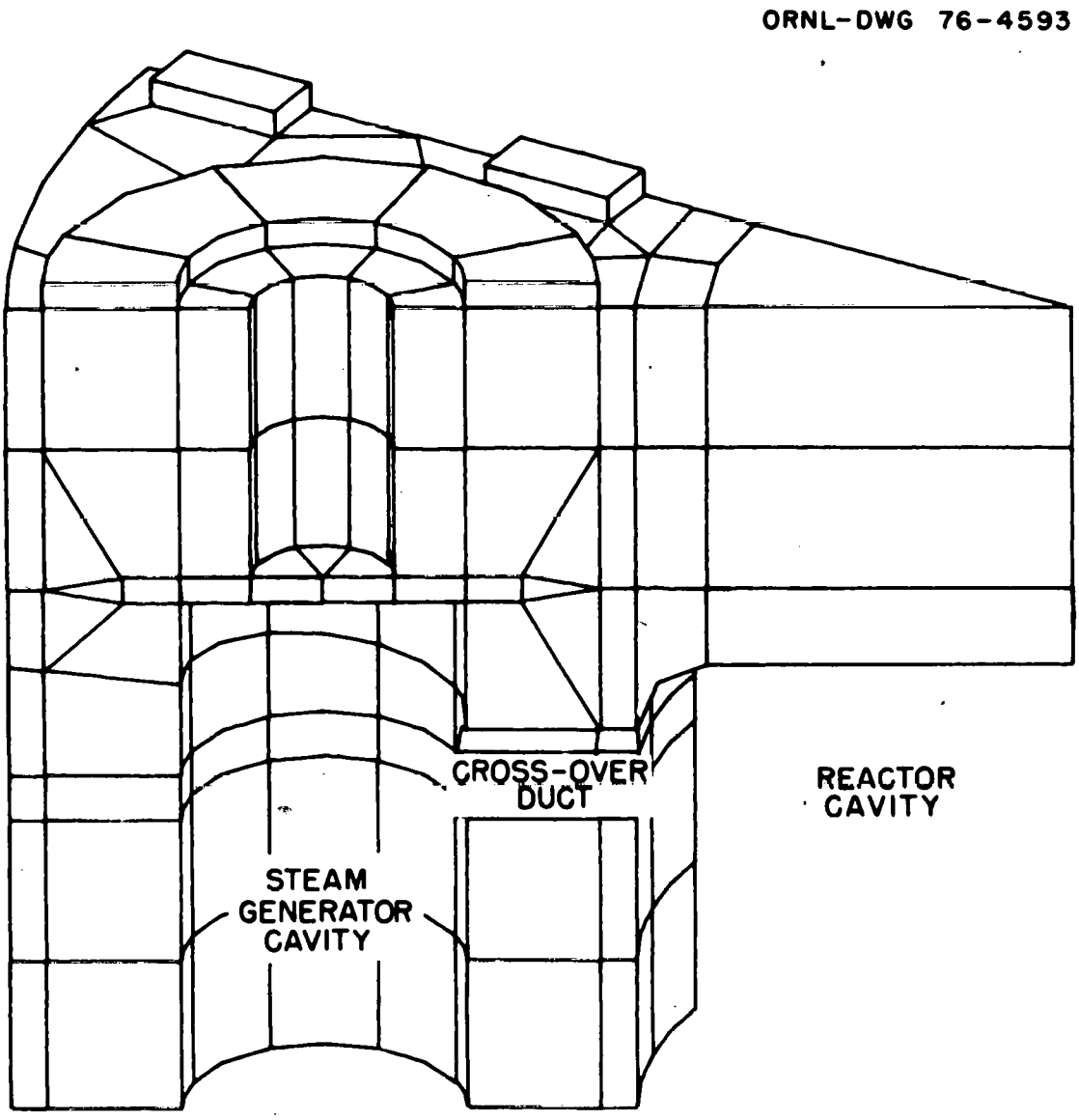

Fig. 9. Analytical model 2 of the Ohbayashi-Gumi vessel.

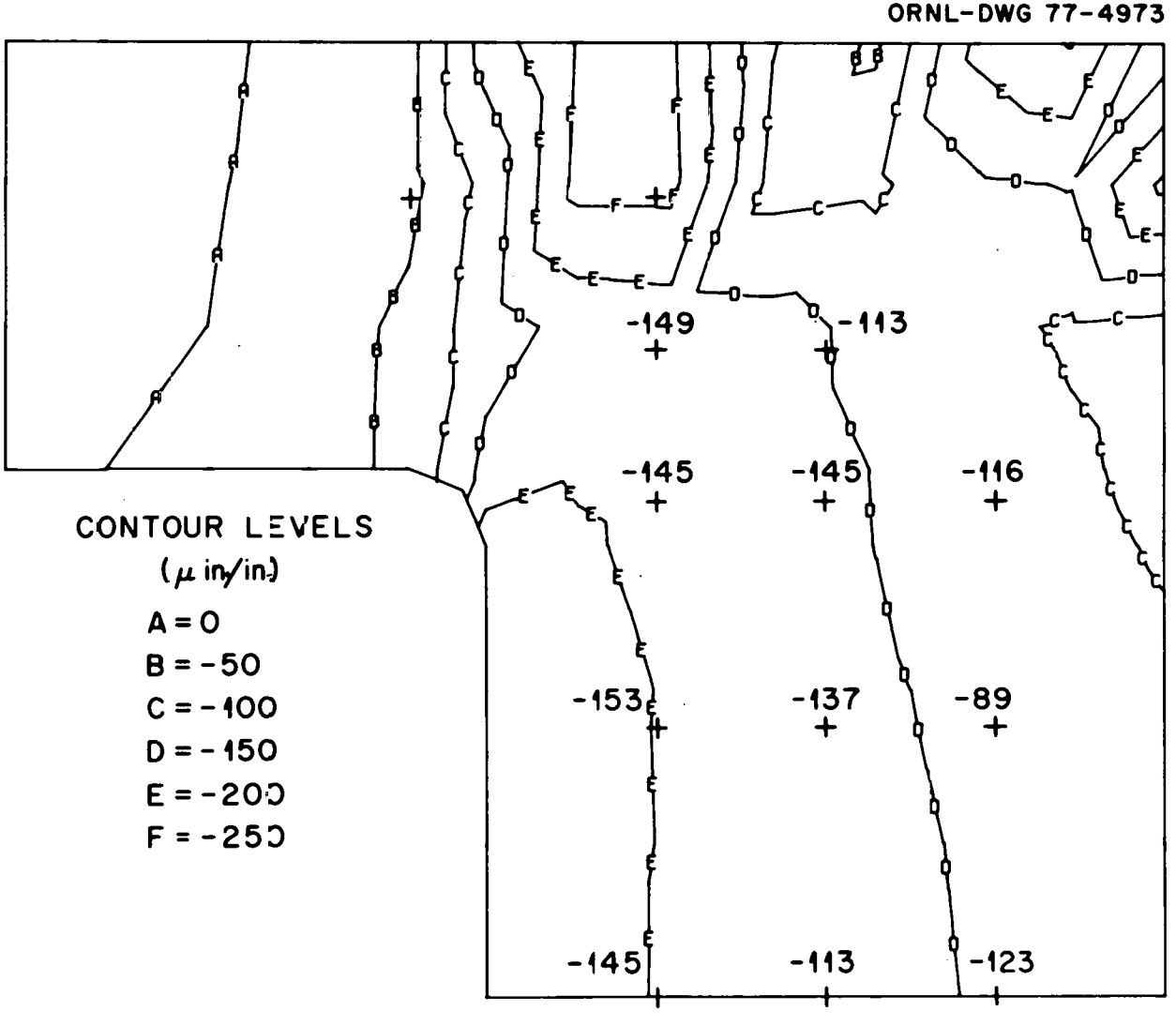

Fig. 10. Axial strains due to vertical prestressing for Ohbayashi-Gumi model 2. (Contours represent calculated values and points represent experimental values in millionths.)

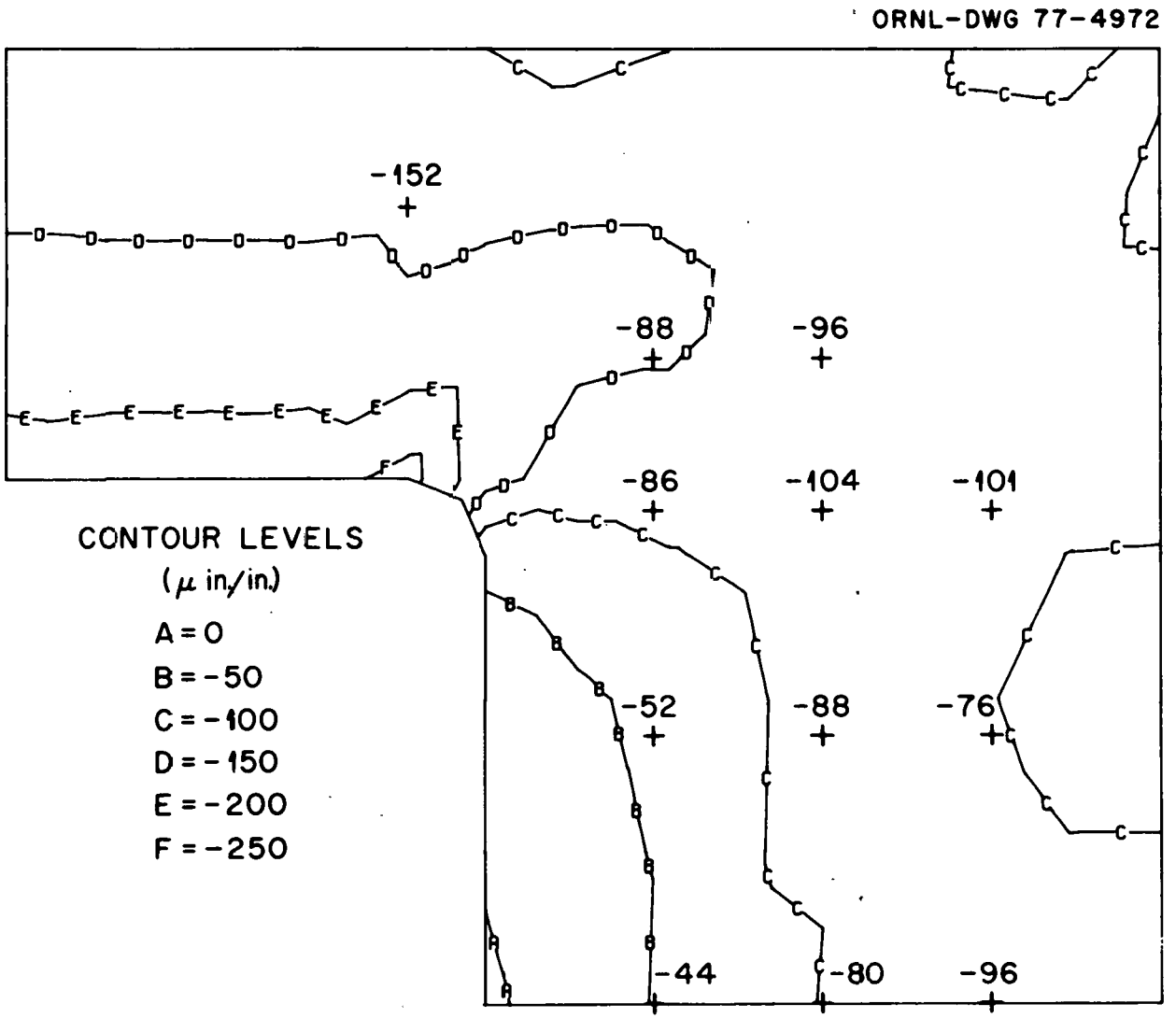

Fig. 11. Radial strains due to circumferential prestressing for Ohbayashi-Gumi model 2. (Contours represent calculated values and points represent experimental values in millionths.)

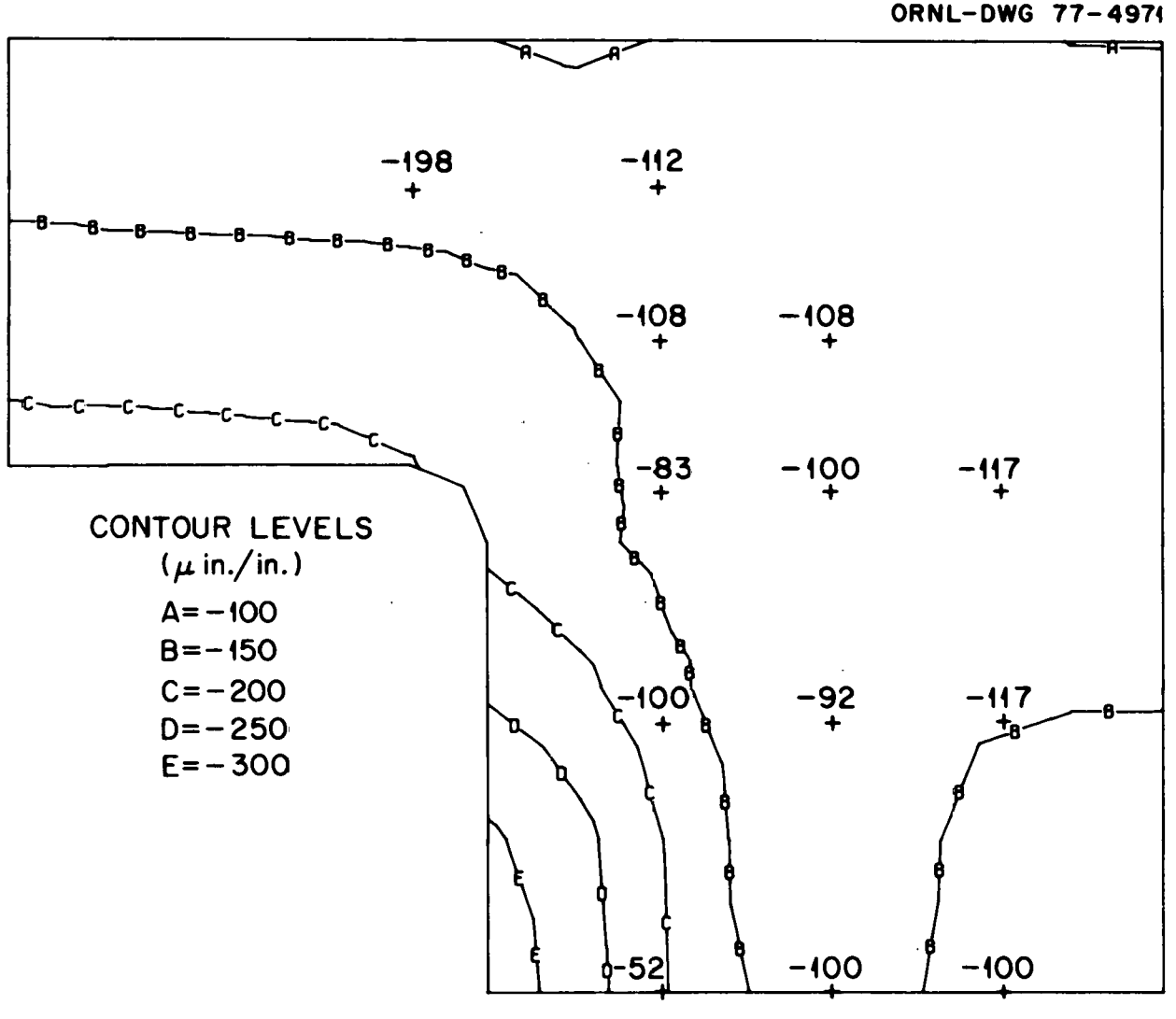

Fig. 12. Hoop strains due to circumferential prestressing for Ohbayashi-Gumi model 2. (Contours represent calculated values and points represent experimental values in millionths.)

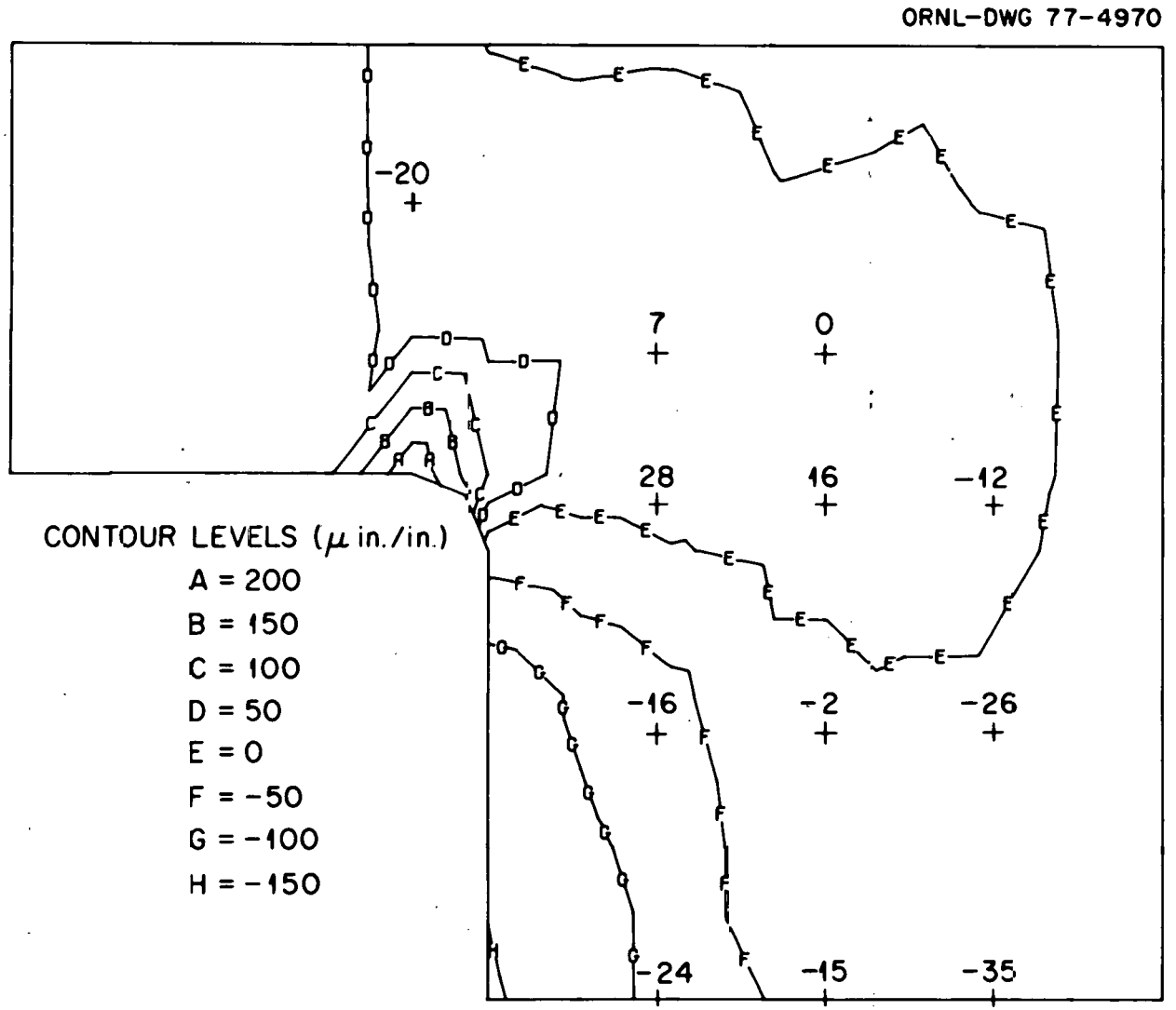

Fig. 13. Radial strains due to design pressure for Ohbayashi-Gumi model 2. (Contours represent calculated values and points represent experimental values in millionths.)

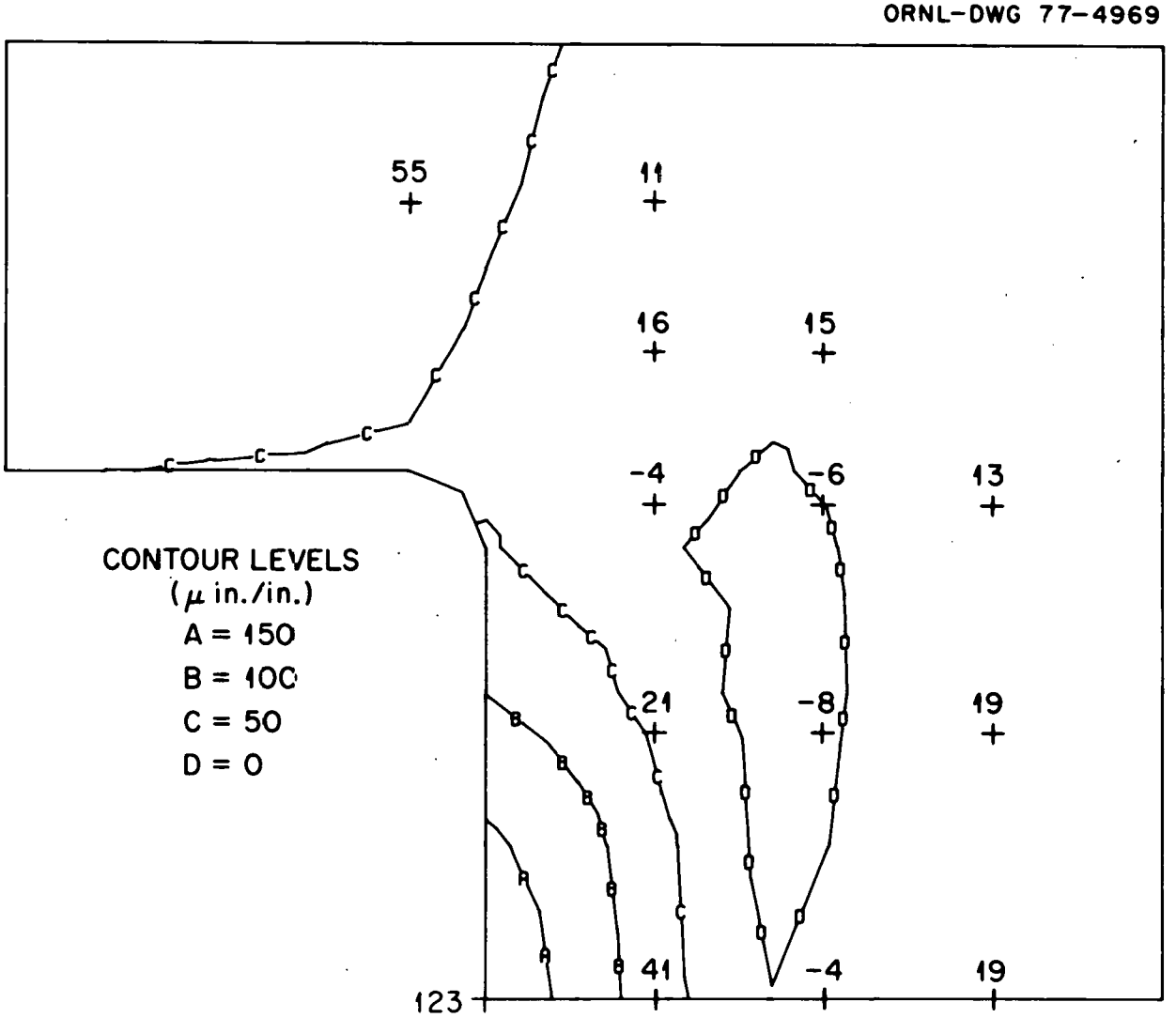

Fig. 14. Hoop strains due to design pressure for Ohbayashi-Gumi model 2. (Contours represent calculated values and points represent experimental values in millionths.)

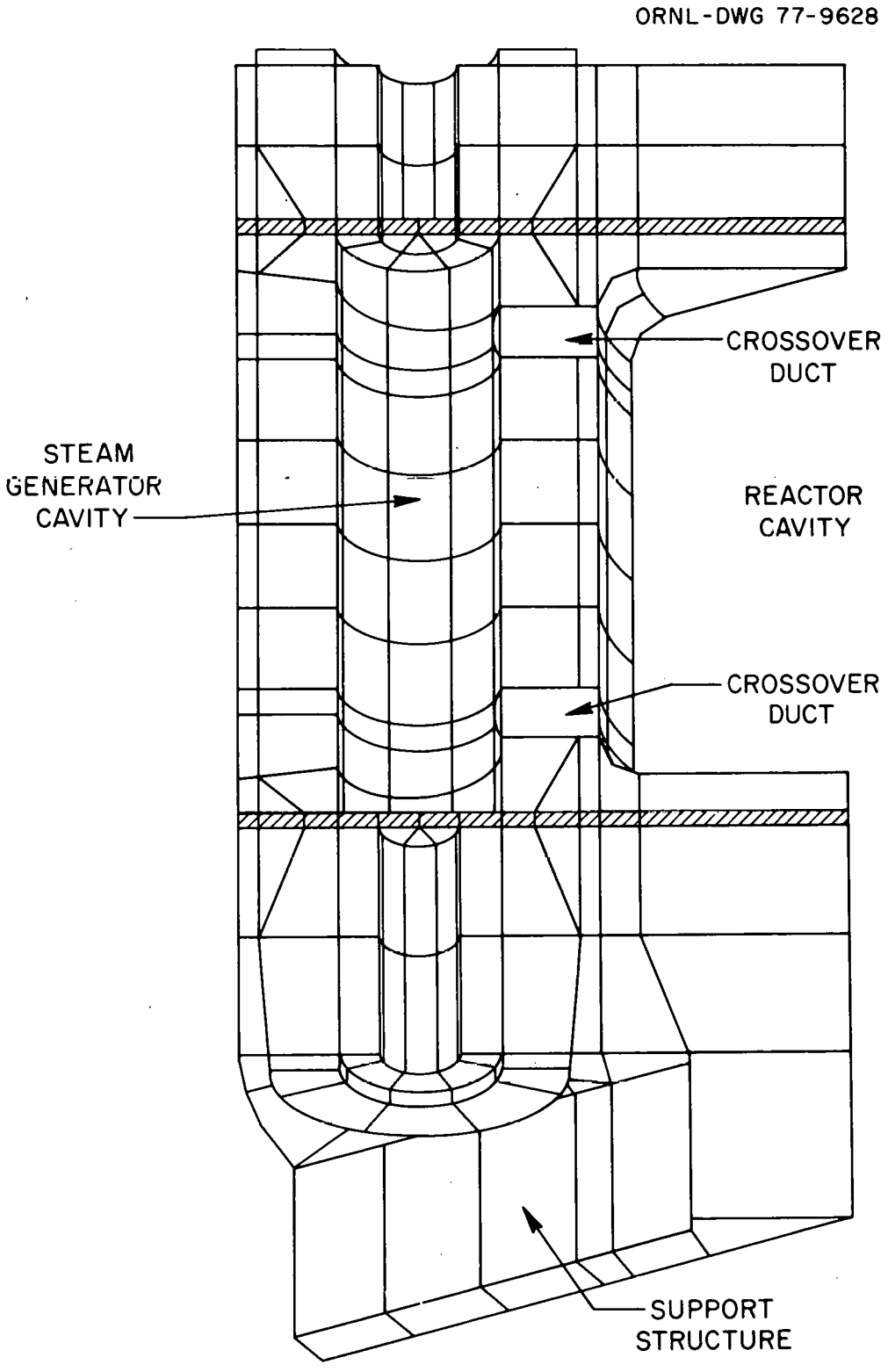

Fig. 15. Analytical model 3 of the Ohbayashi-Gumi vessel.

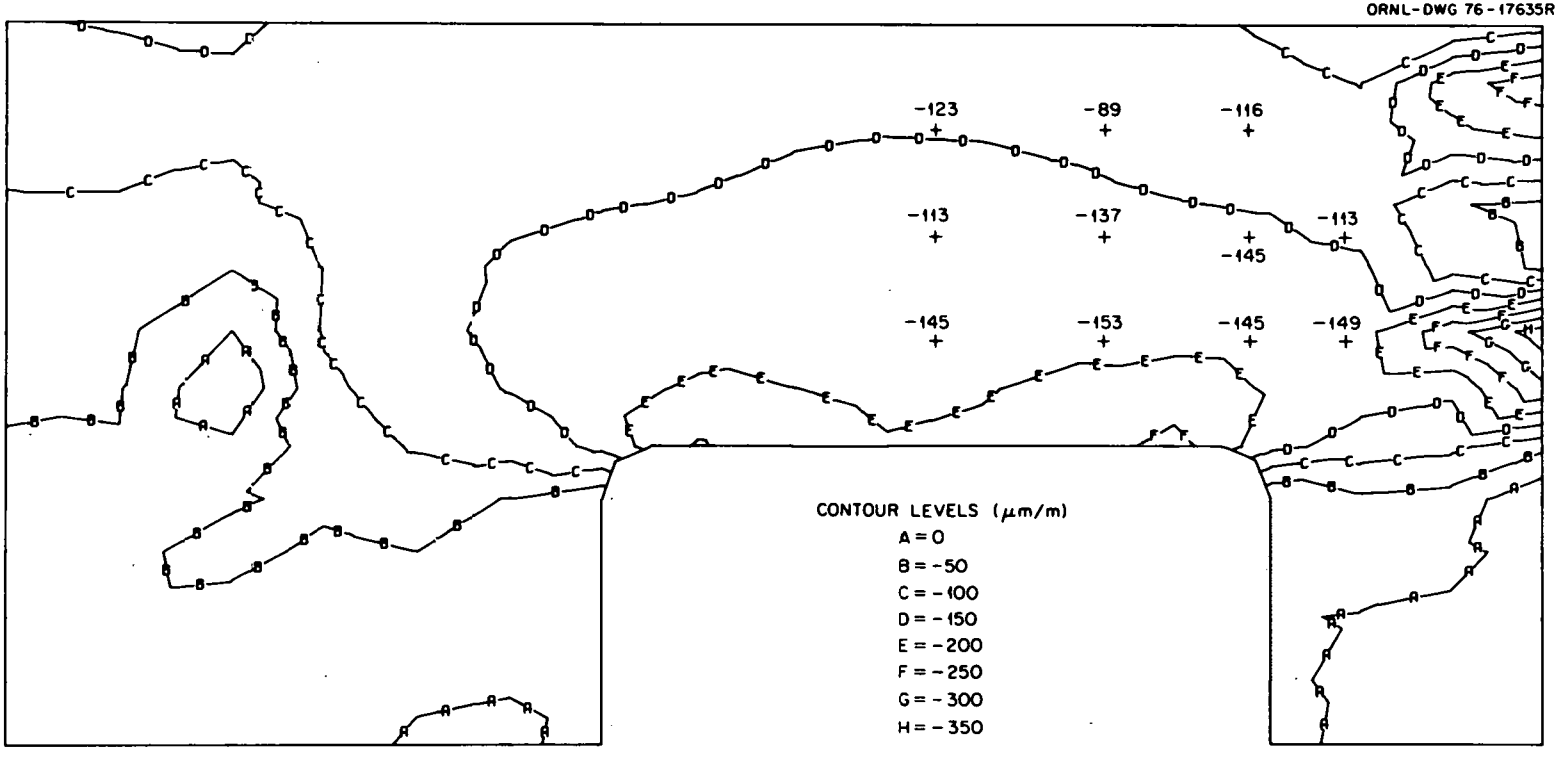

Fig. 16. Axial strains due to vertical prestressing for Ohbayashi-Gumi model 3. (Contours represent calculated values and points represent experimental values in millionths.)

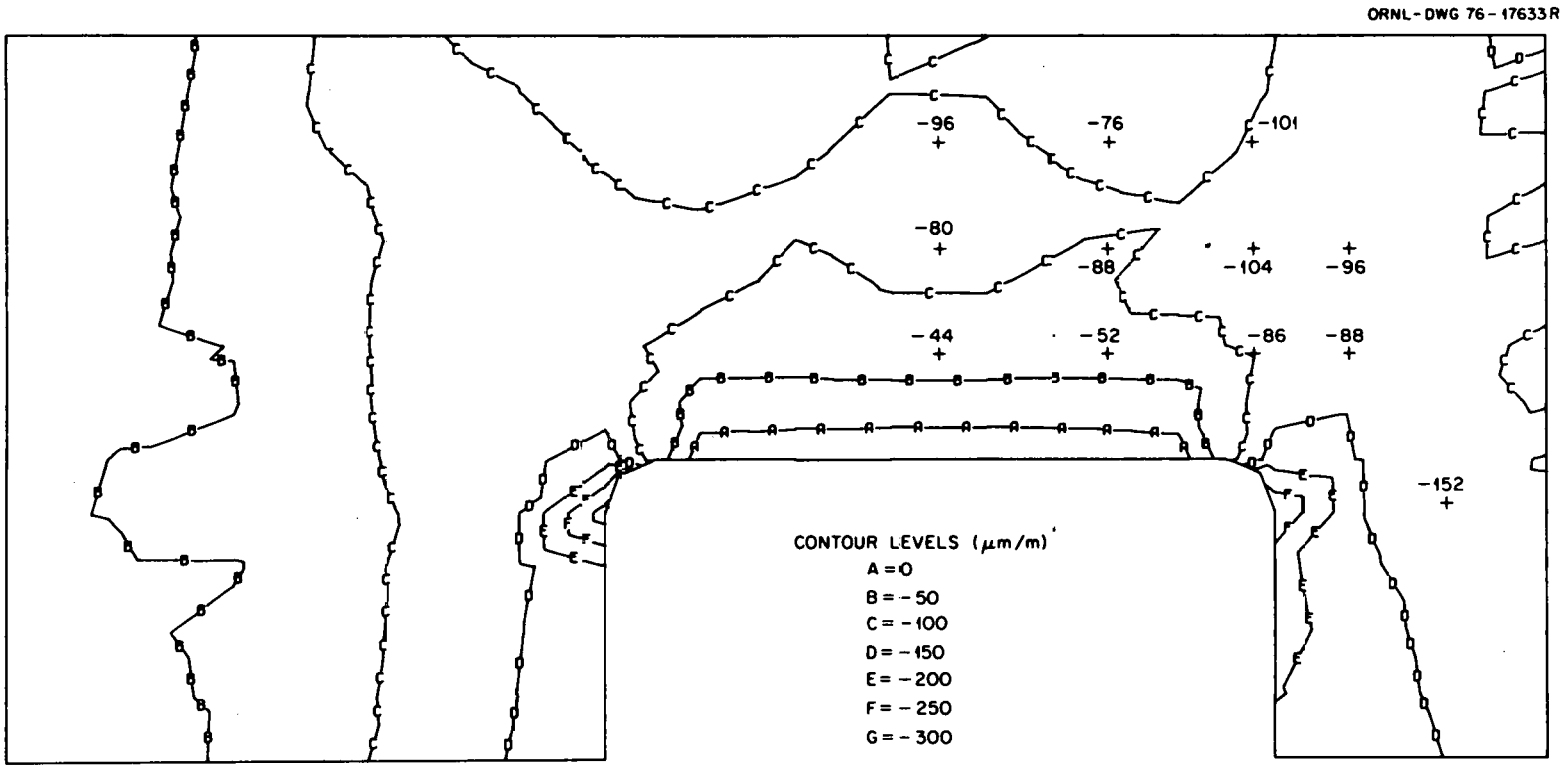

Fig. 17. Radial strains due to circumferential prestressing for Ohbayashi-Gumi model 3. (Contours represent calculated values and points represent experimental values in millionths.)

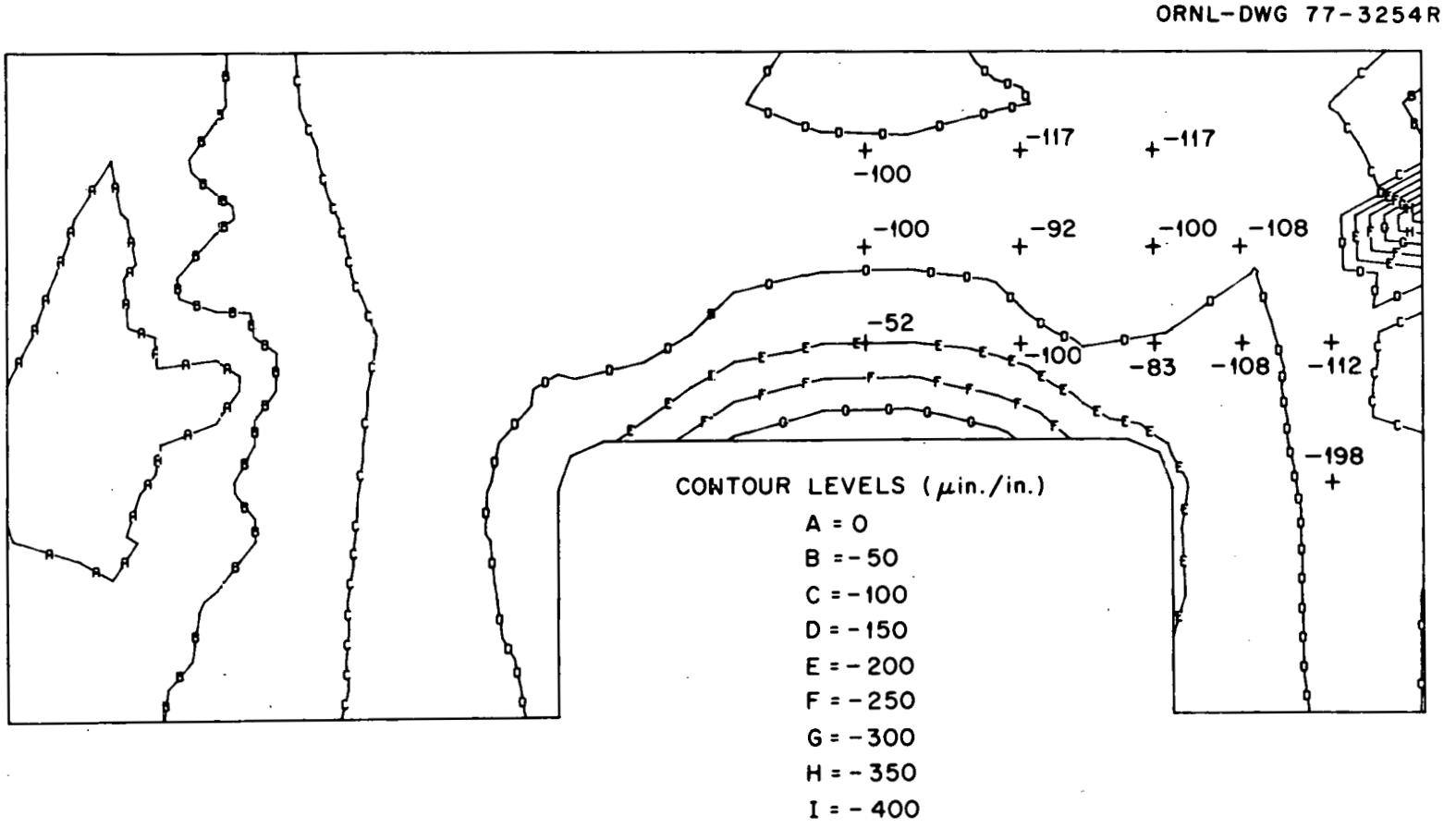

Fig. 18. Hoop strains due to circumferential prestressing for Ohbayashi-Gumi model 3. (Contours represent calculated values and points represent experimental values in millionths.)

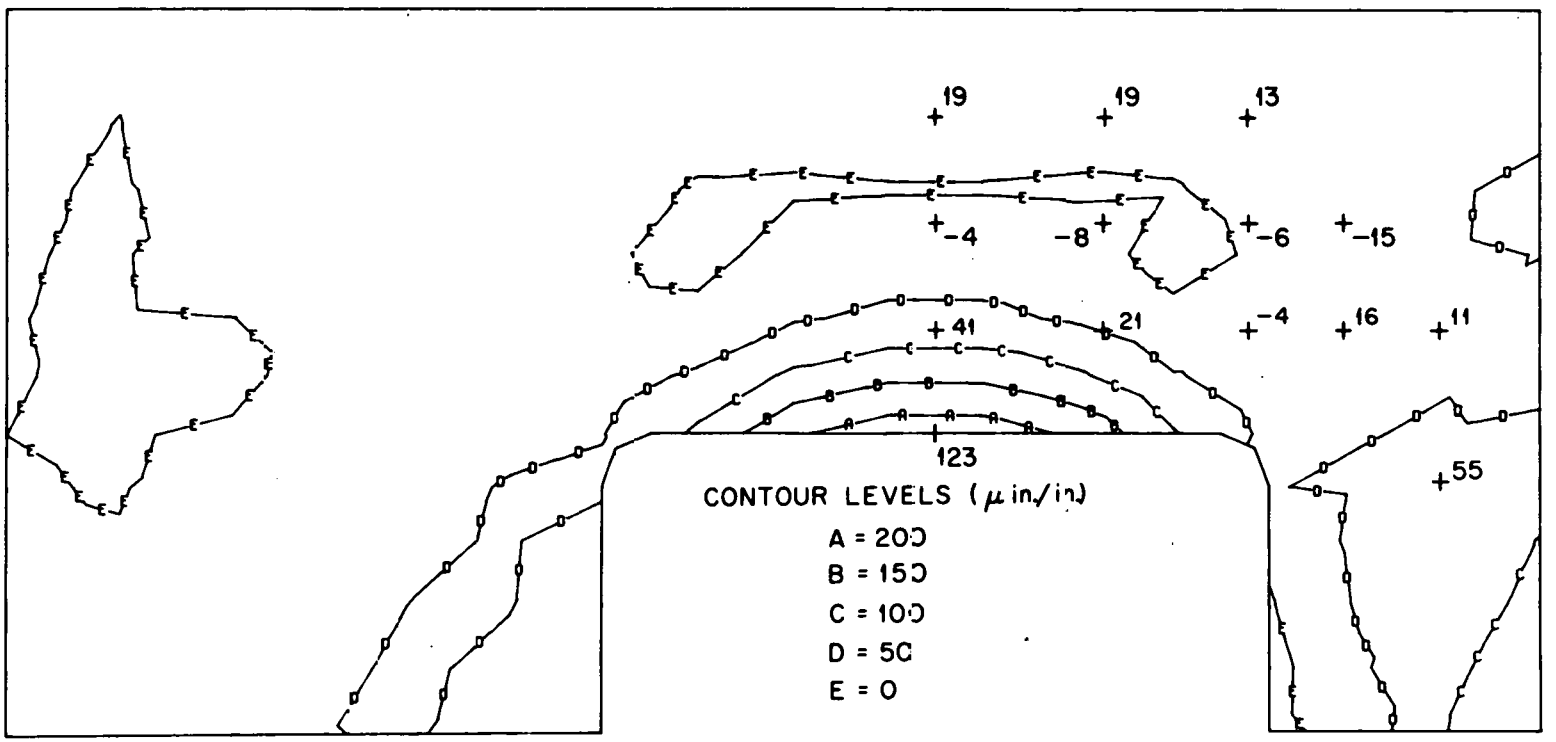

Fig. 19. Hoop strains due to design pressure for Ohbayashi-Gumi model 3. (Contours represent calculated values and points represent experimental values in millionths.)

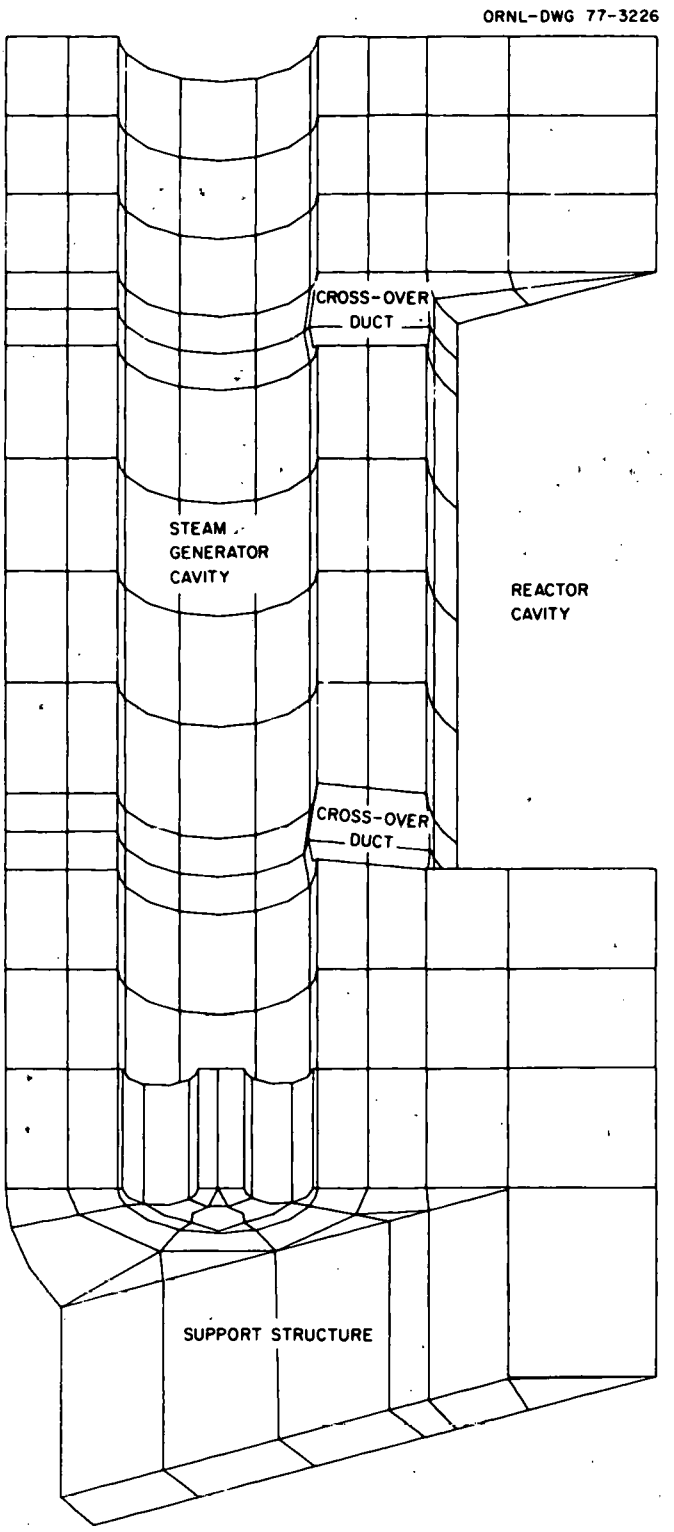

Fig. 20. Analytical model for PCRV designed for a commercial HTGR.

ORNL-DWG 77-9361

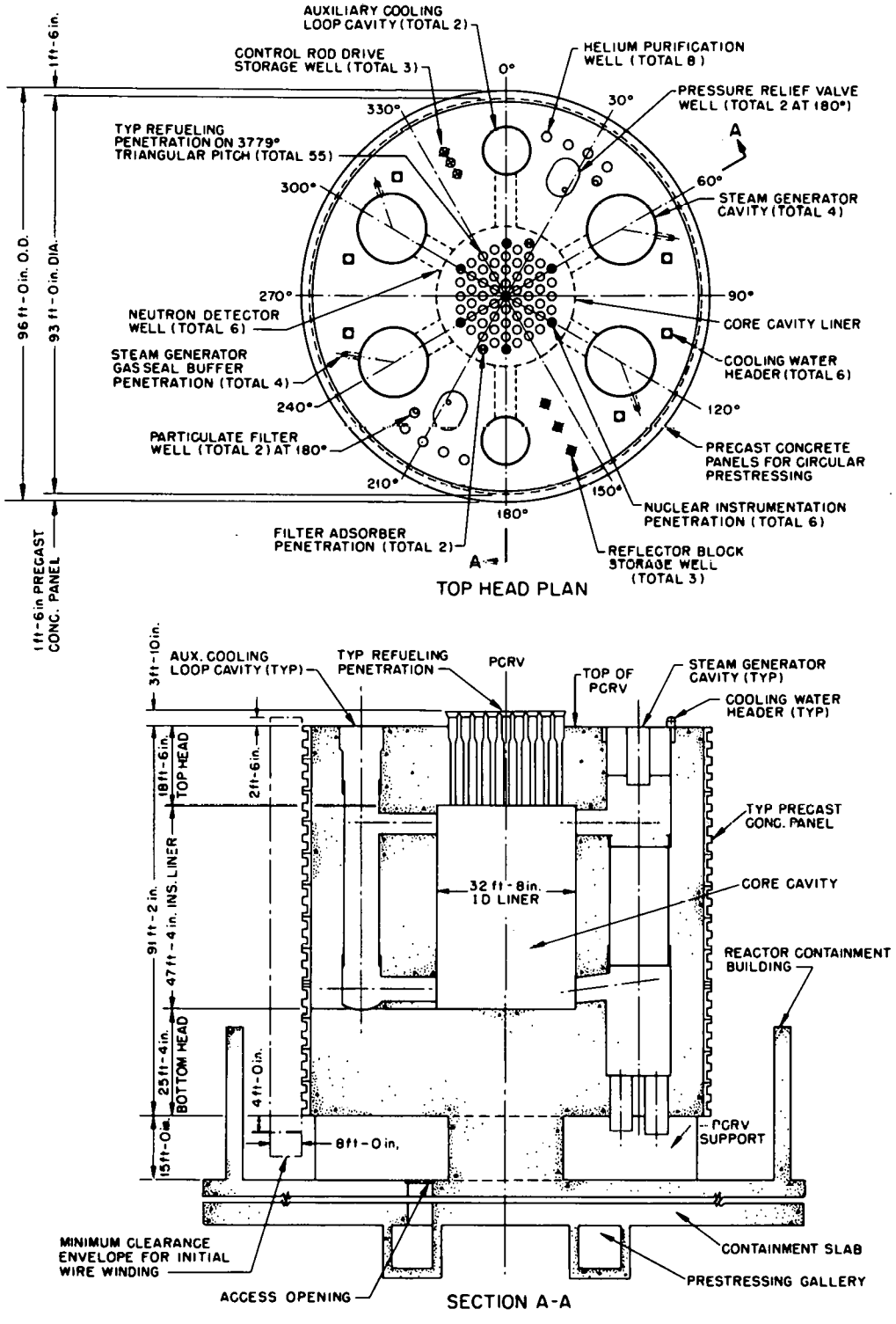

Fig. 21. General arrangement of PCRV for a commercial HTGR.

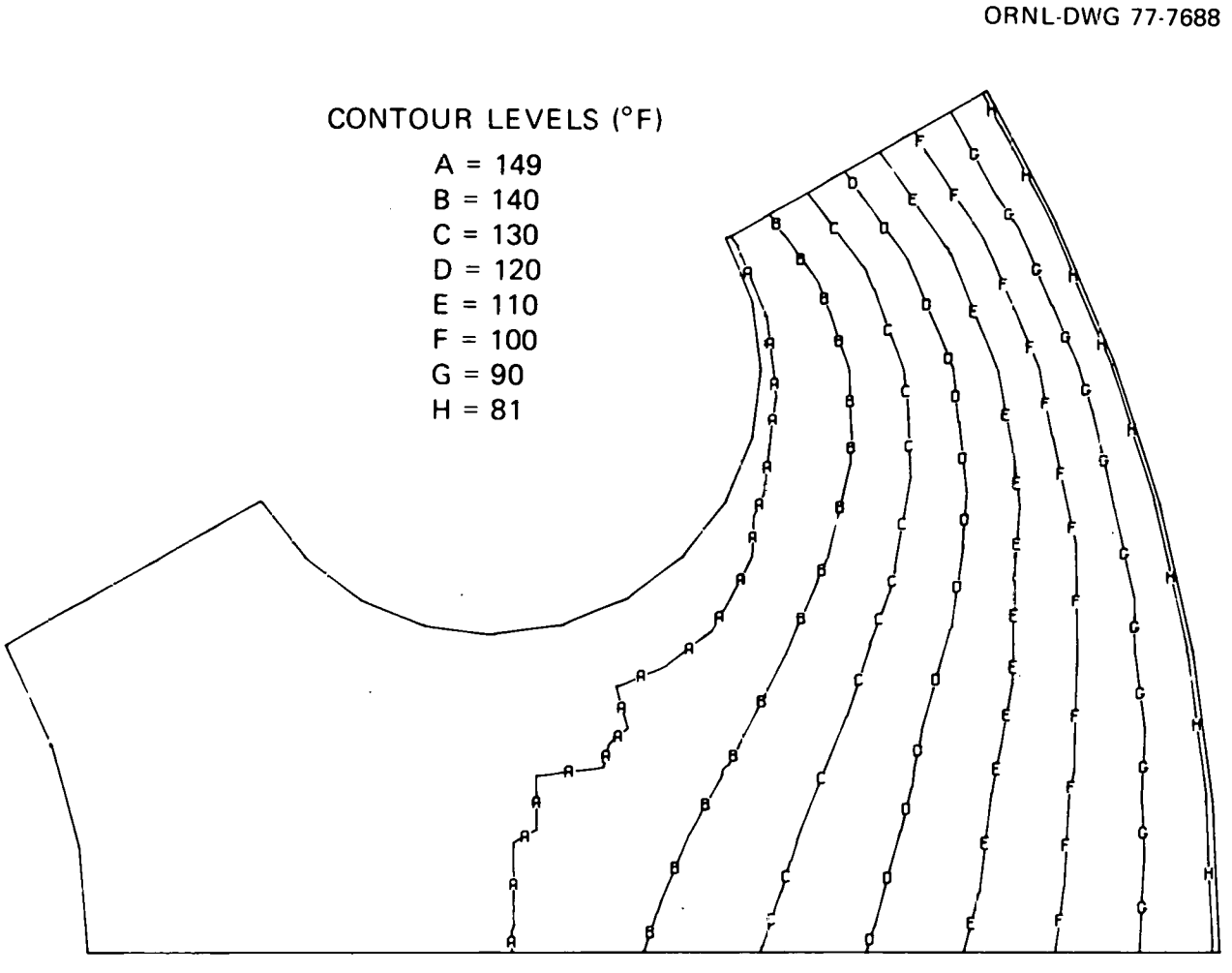

Fig. 22. Isotherms on horizontal section at midheight of reactor cavity of the HTGR vessel.

ORNL-DWG 77-7687

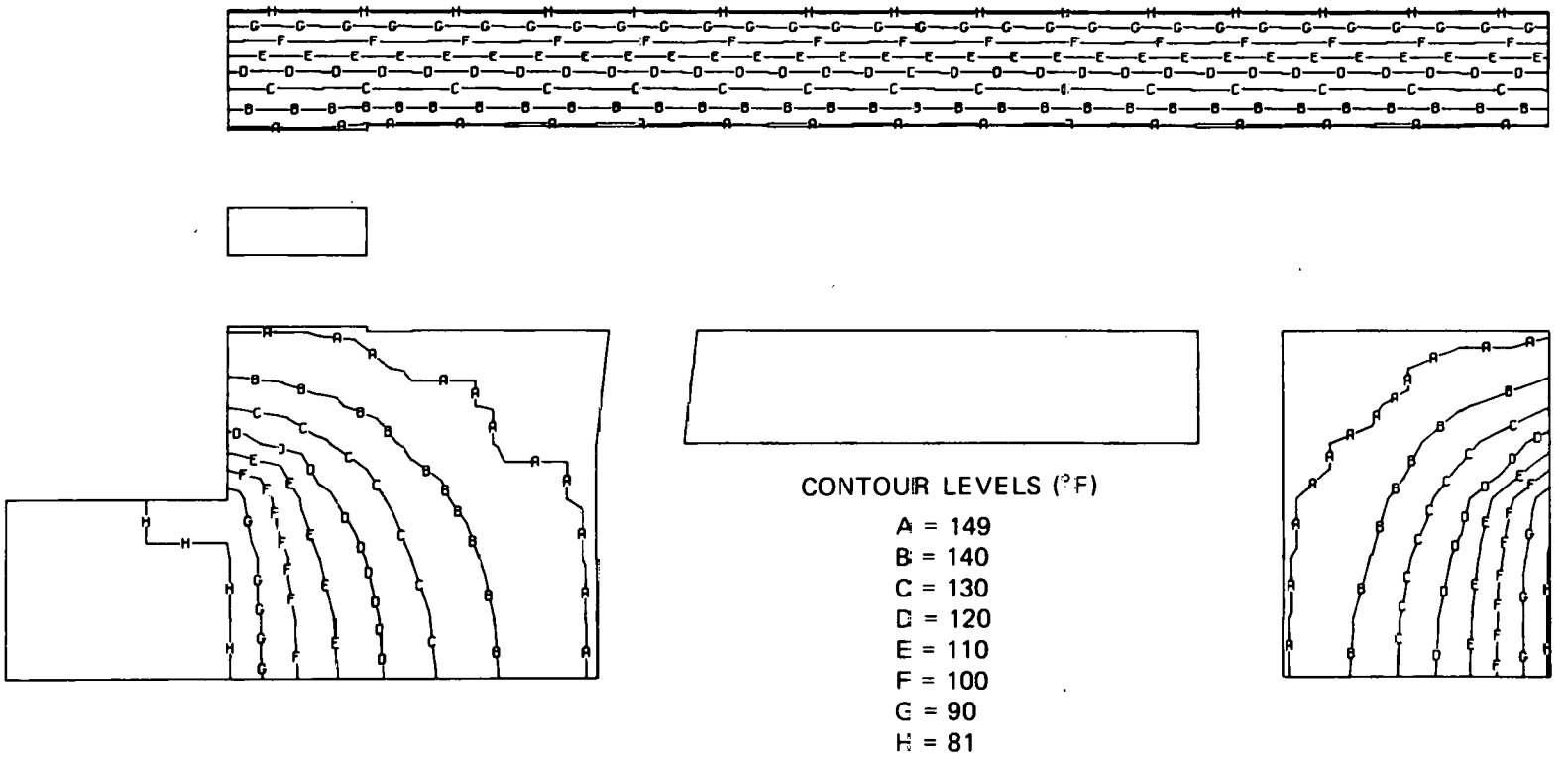

Fig. 23. Isotherms on vertical section through steam-generator cavity.

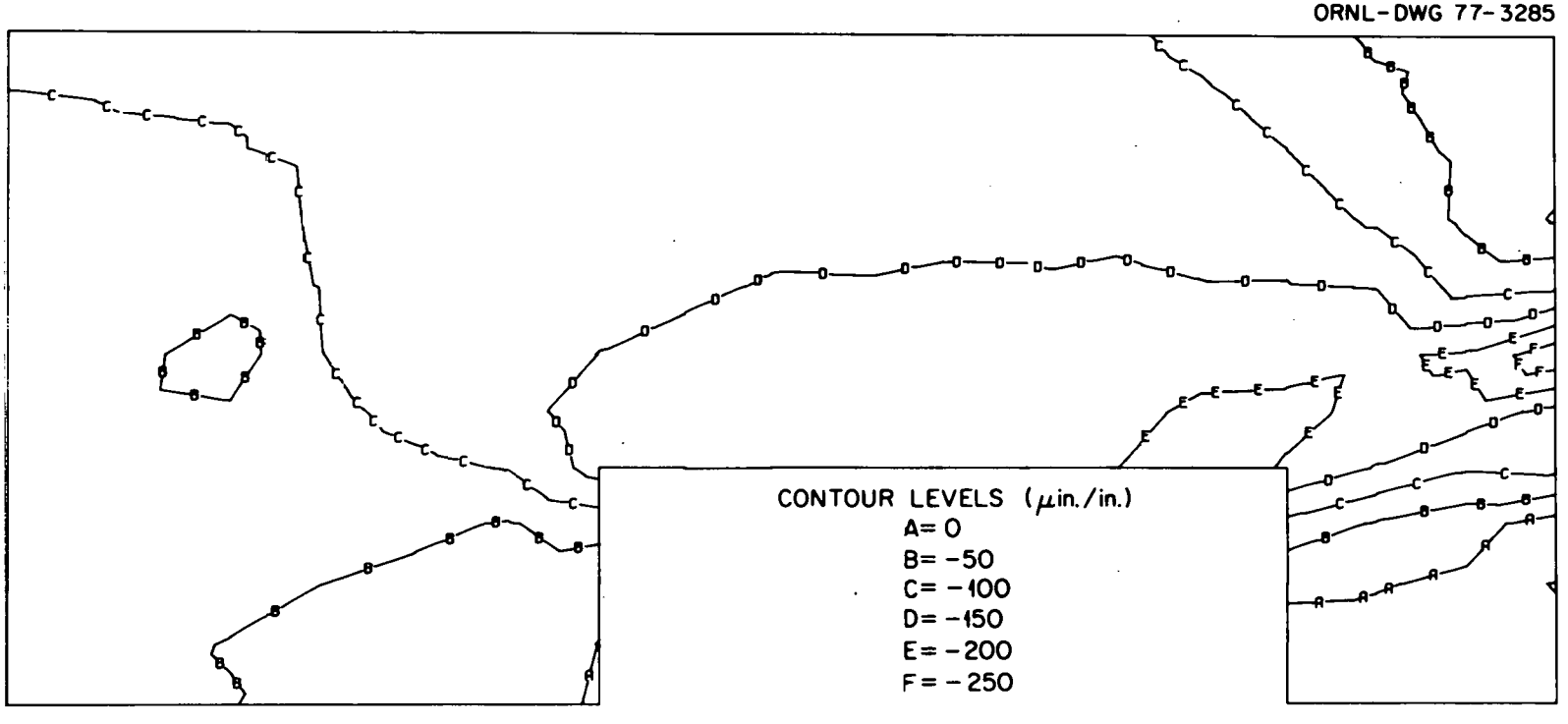

Fig. 24. Axial strain due to vertical prestressing for HTGR vessel.

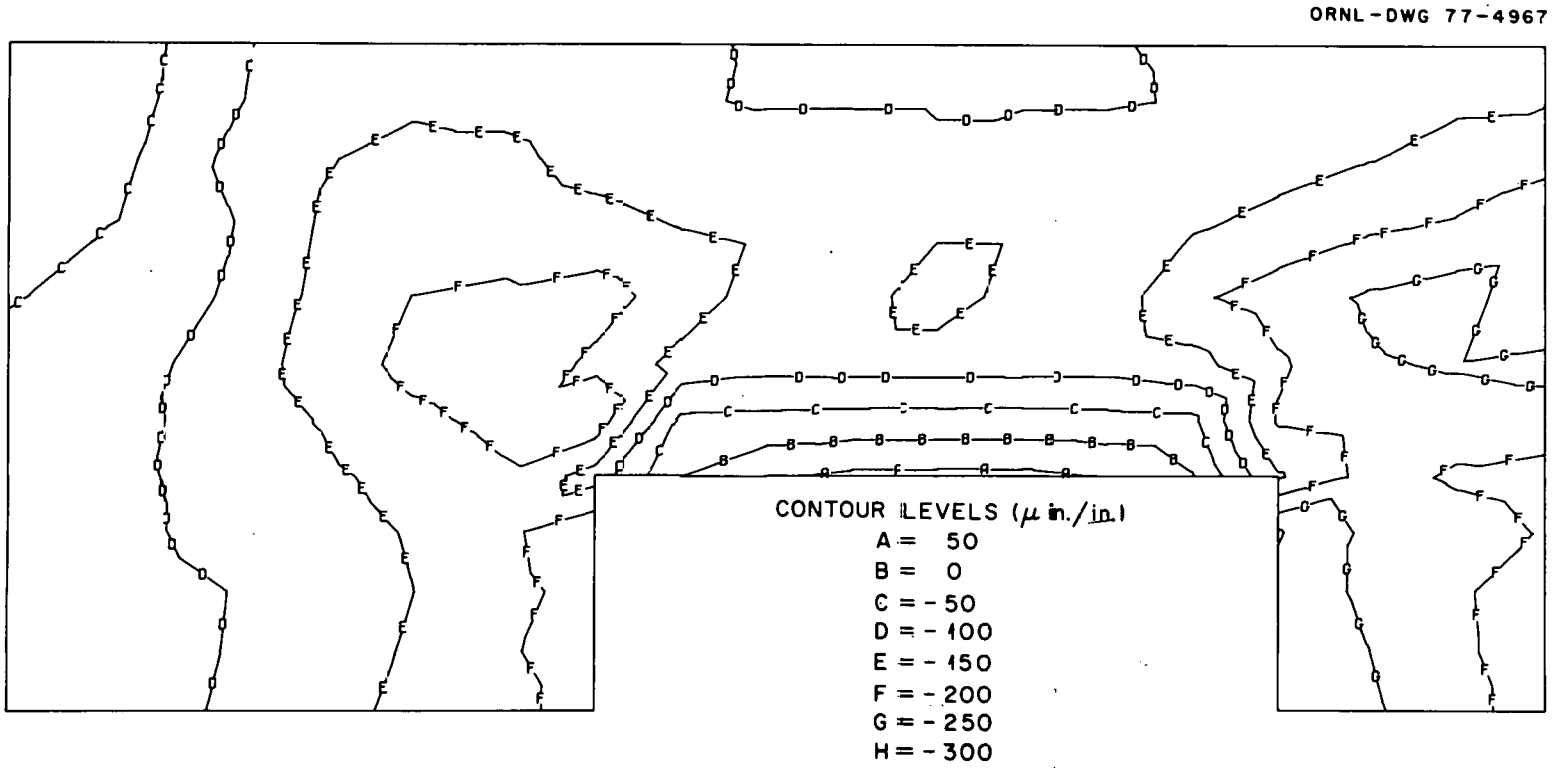

Fig. 25. Radial strain due to circumferential prestressing for HTGR vessel.

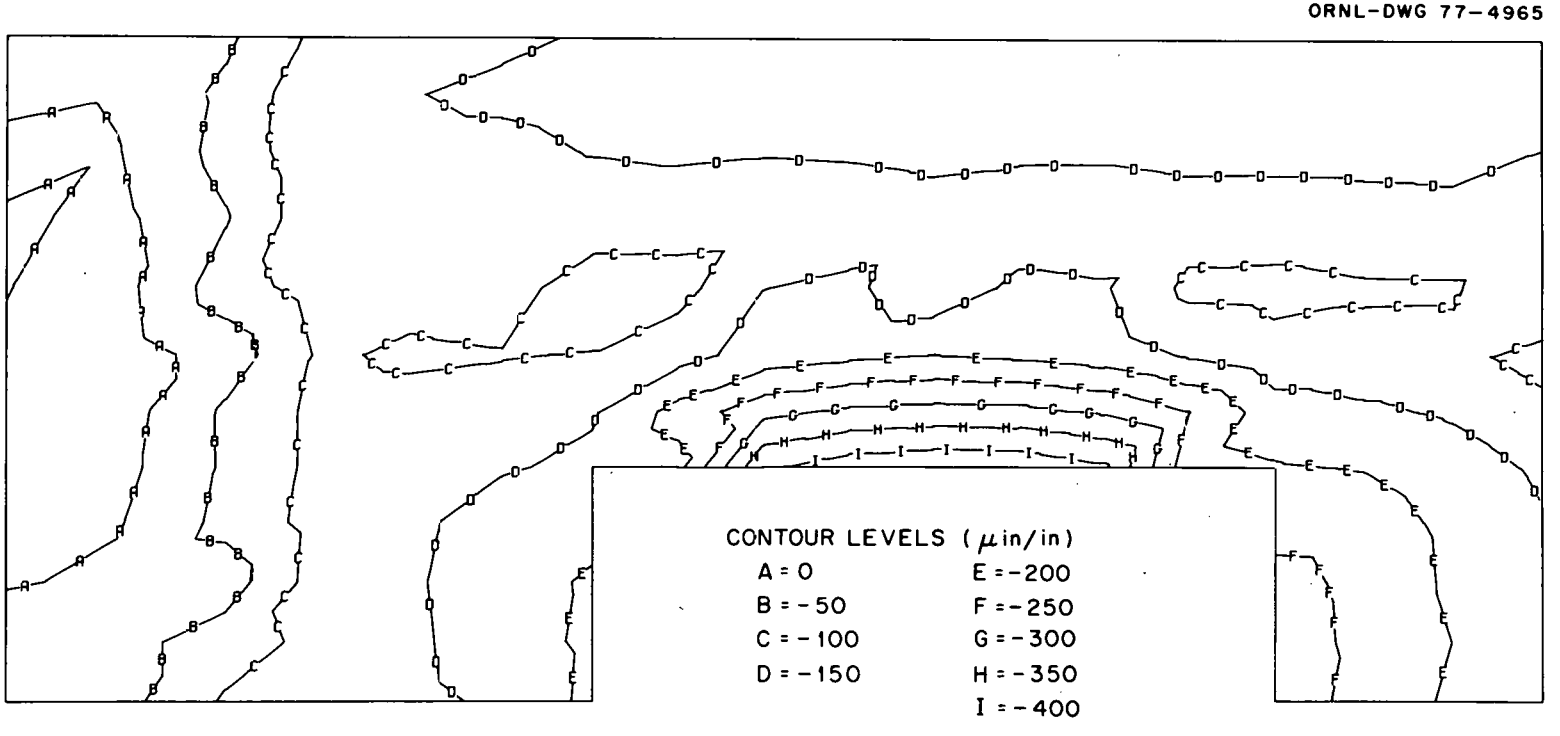

Fig. 26. Hoop strain due to circumferential prestressing for HTGR vessel.

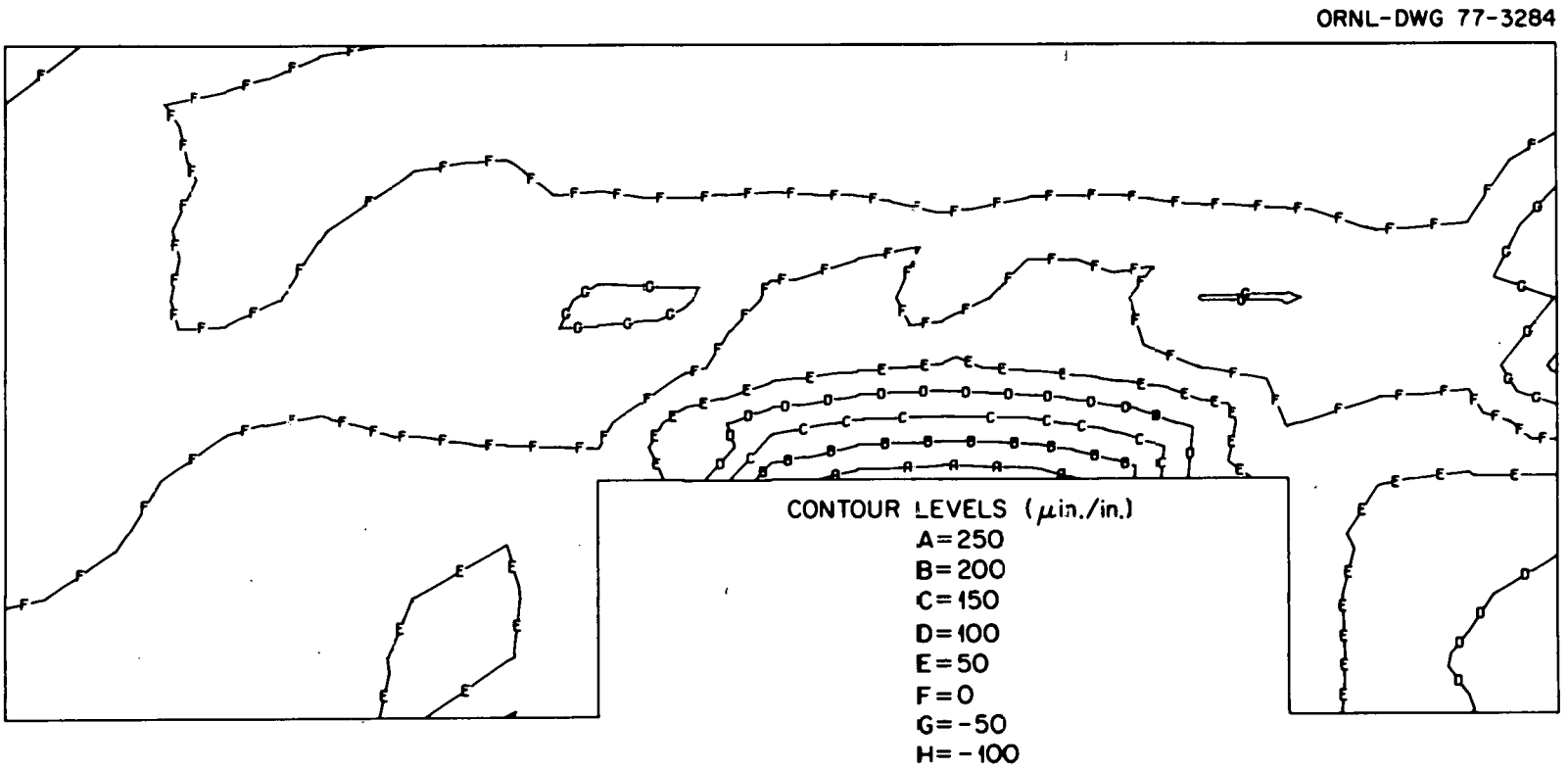

Fig. 27. Hoop strain due to internal pressure for HTGR vessel.

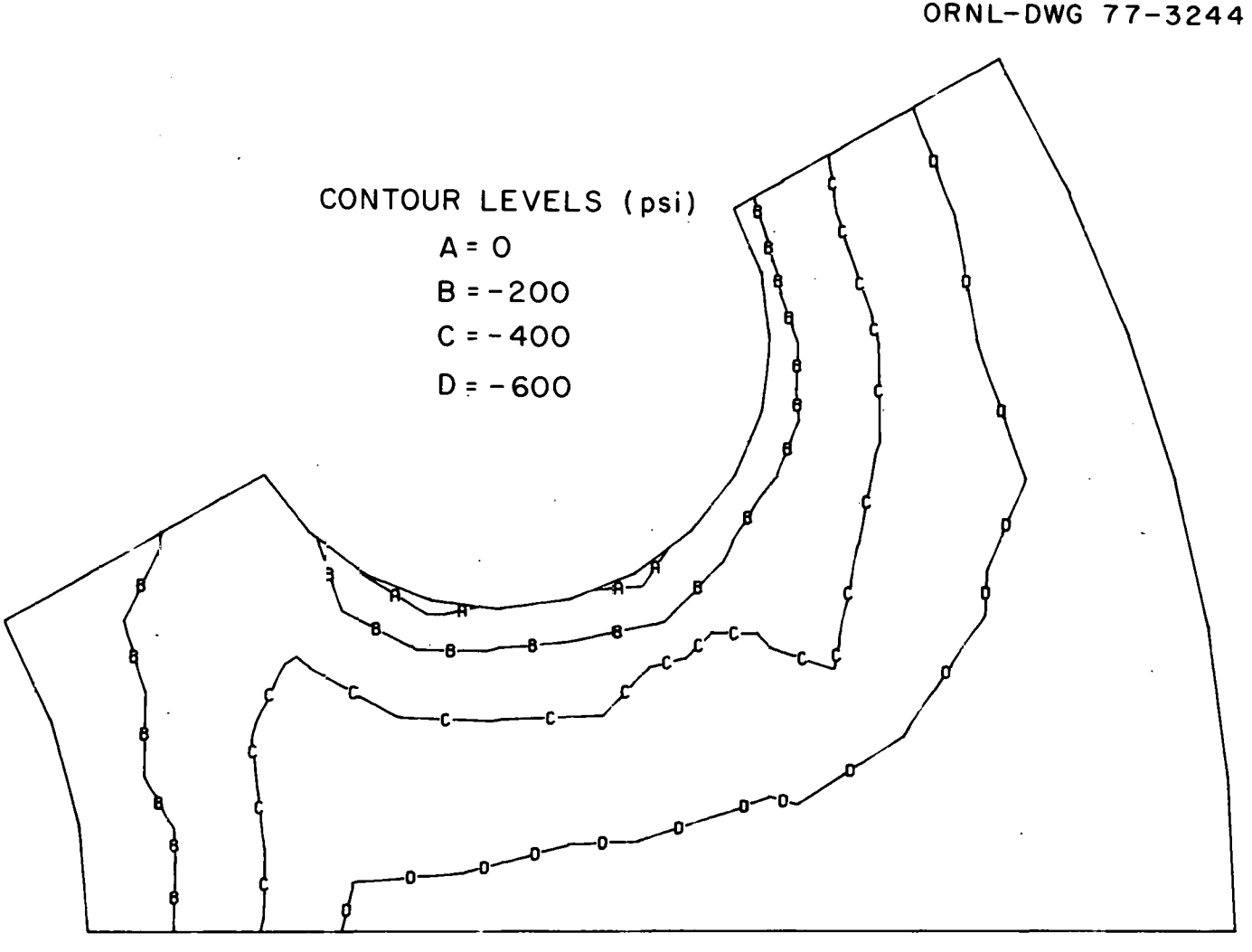

Fig. 28. Maximum principal stress due to initial prestressing for HTGR vessel.

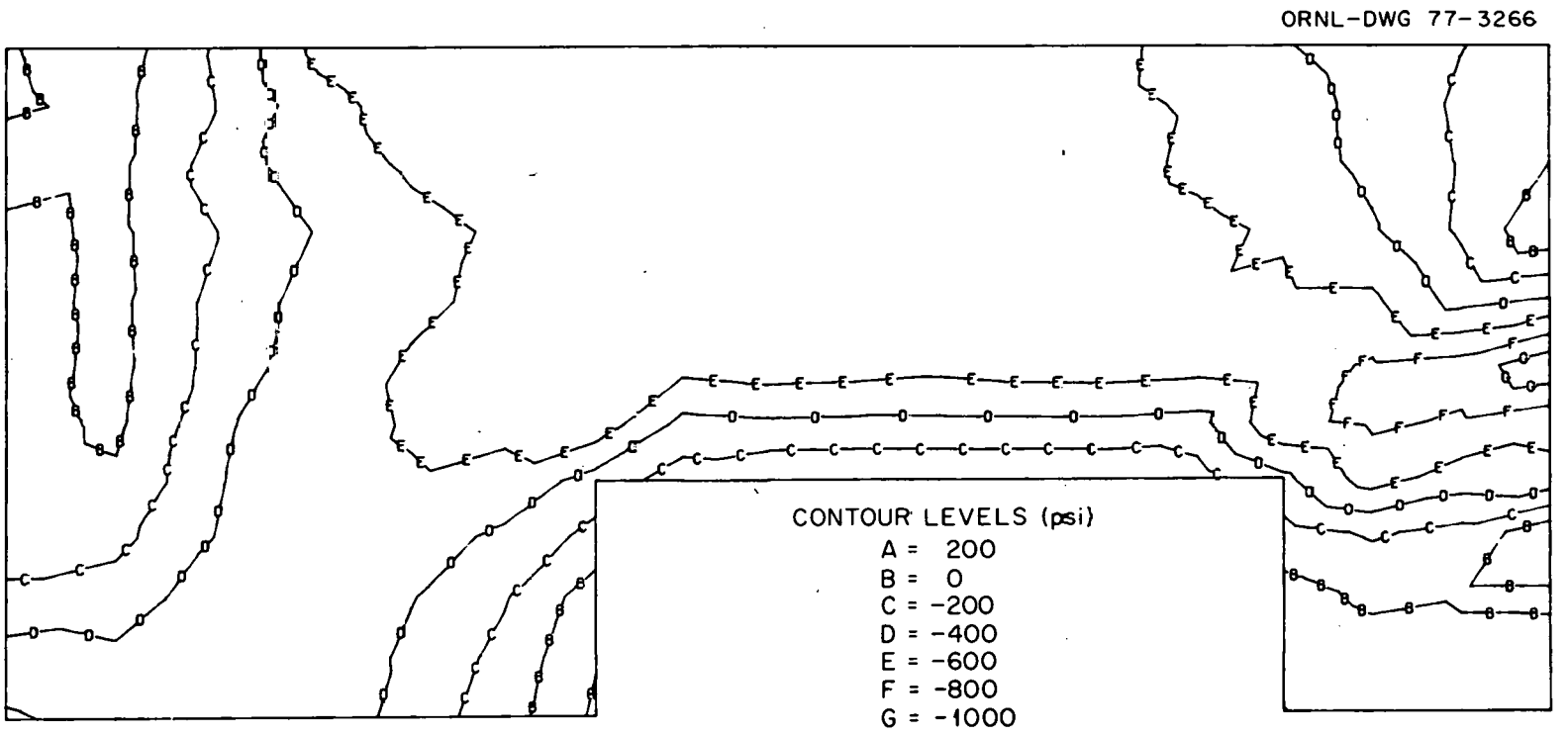

Fig. 29. Maximum principal stress due to initial prestressing for HTGR vessel.

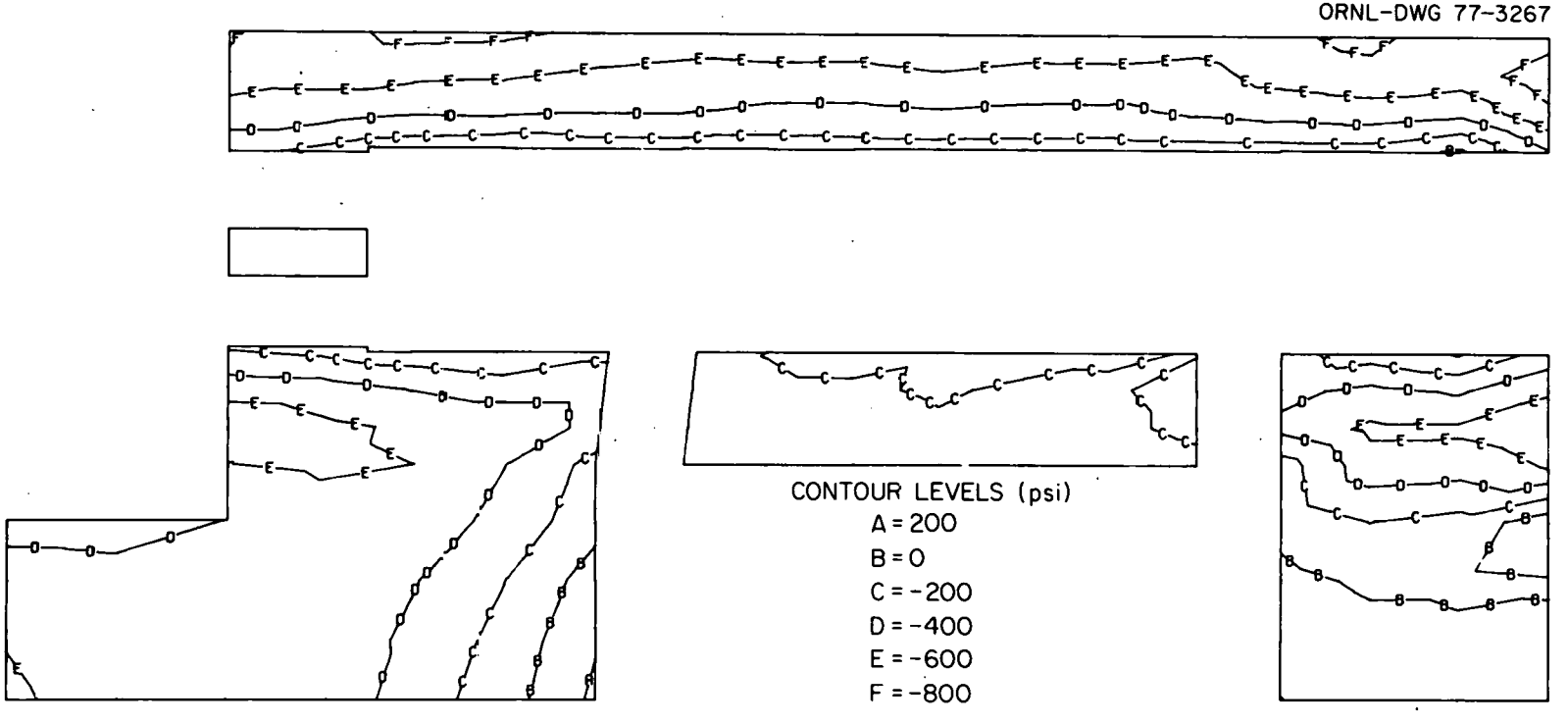

Fig. 30. Maximum principal stress due to initial prestressing for HTGR vessel.

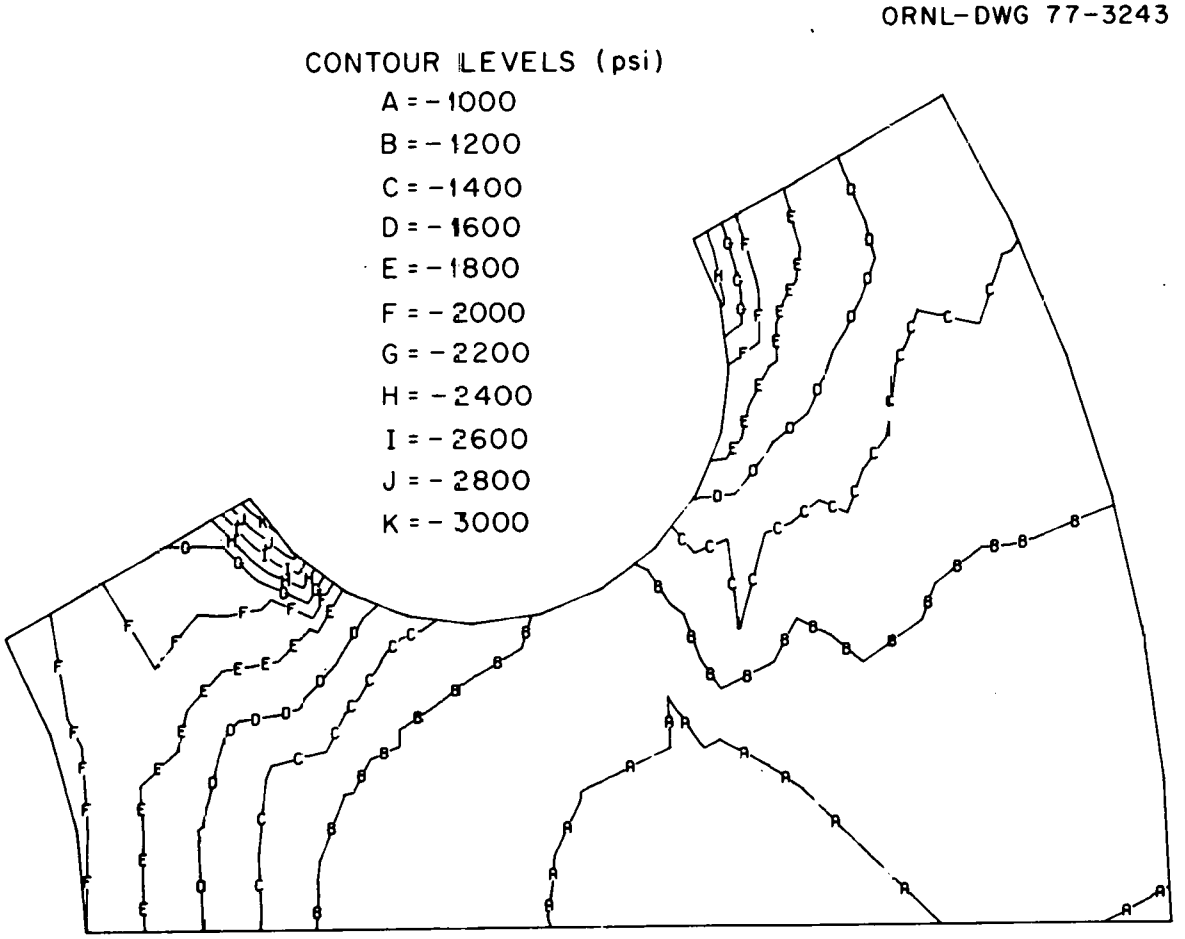

Fig. 31. Minimum principal stress due to initial prestressing for HTGR vessel.

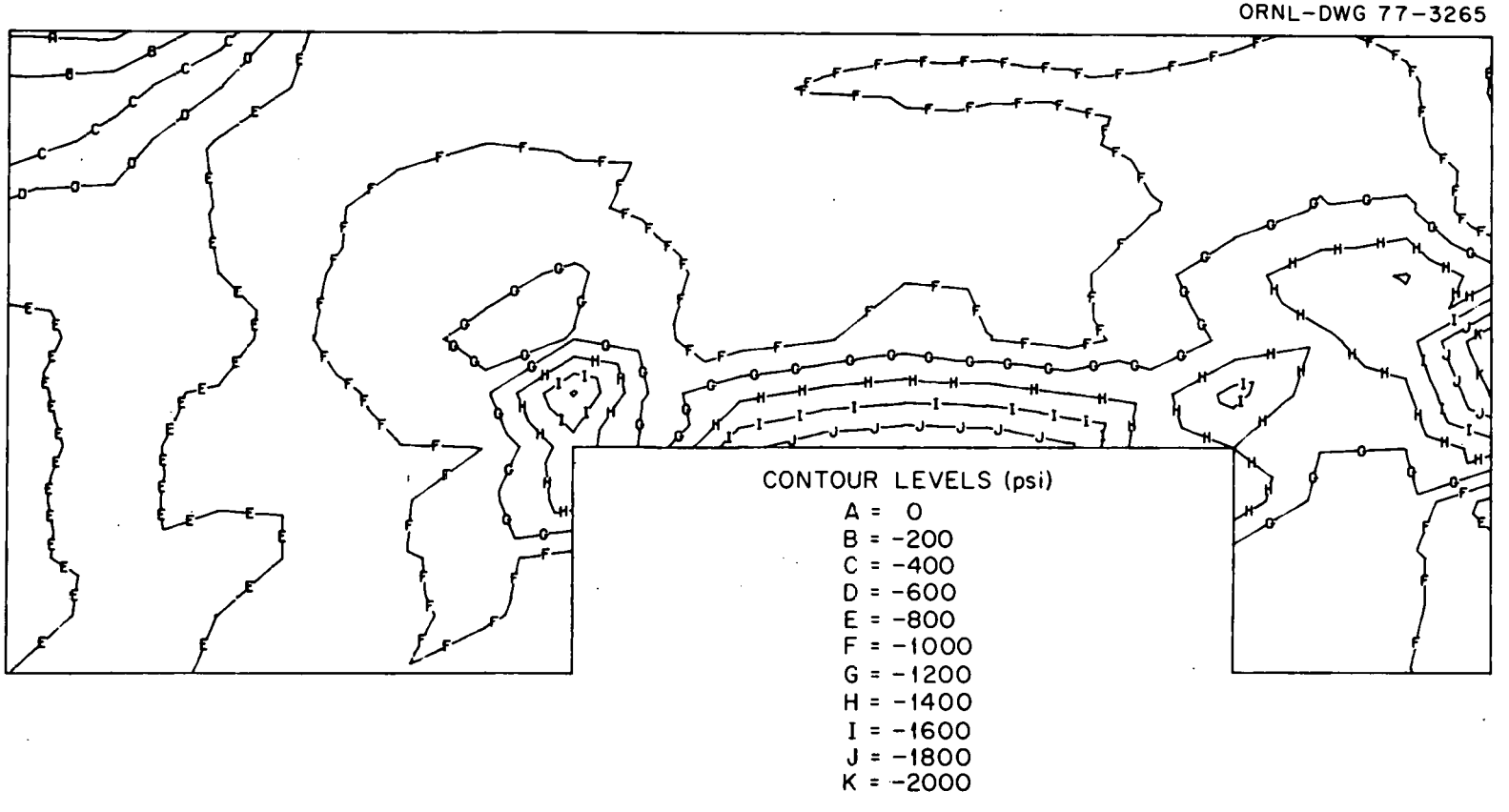

Fig. 32. Minimum principal stress due to initial prestressing for HTGR vessel.

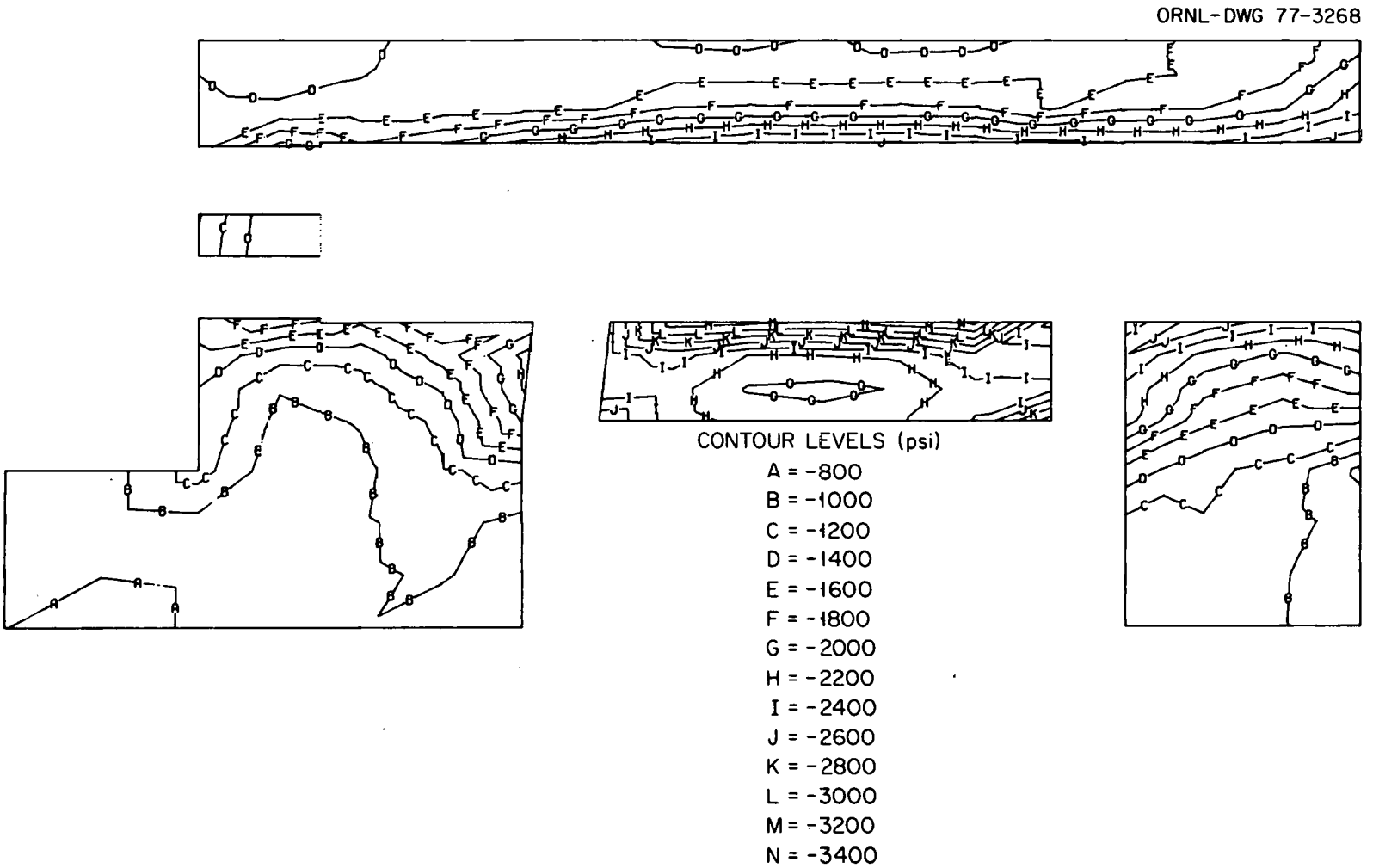

Fig. 33. Minimum principal stress due to initial prestressing for HTGR vessel.

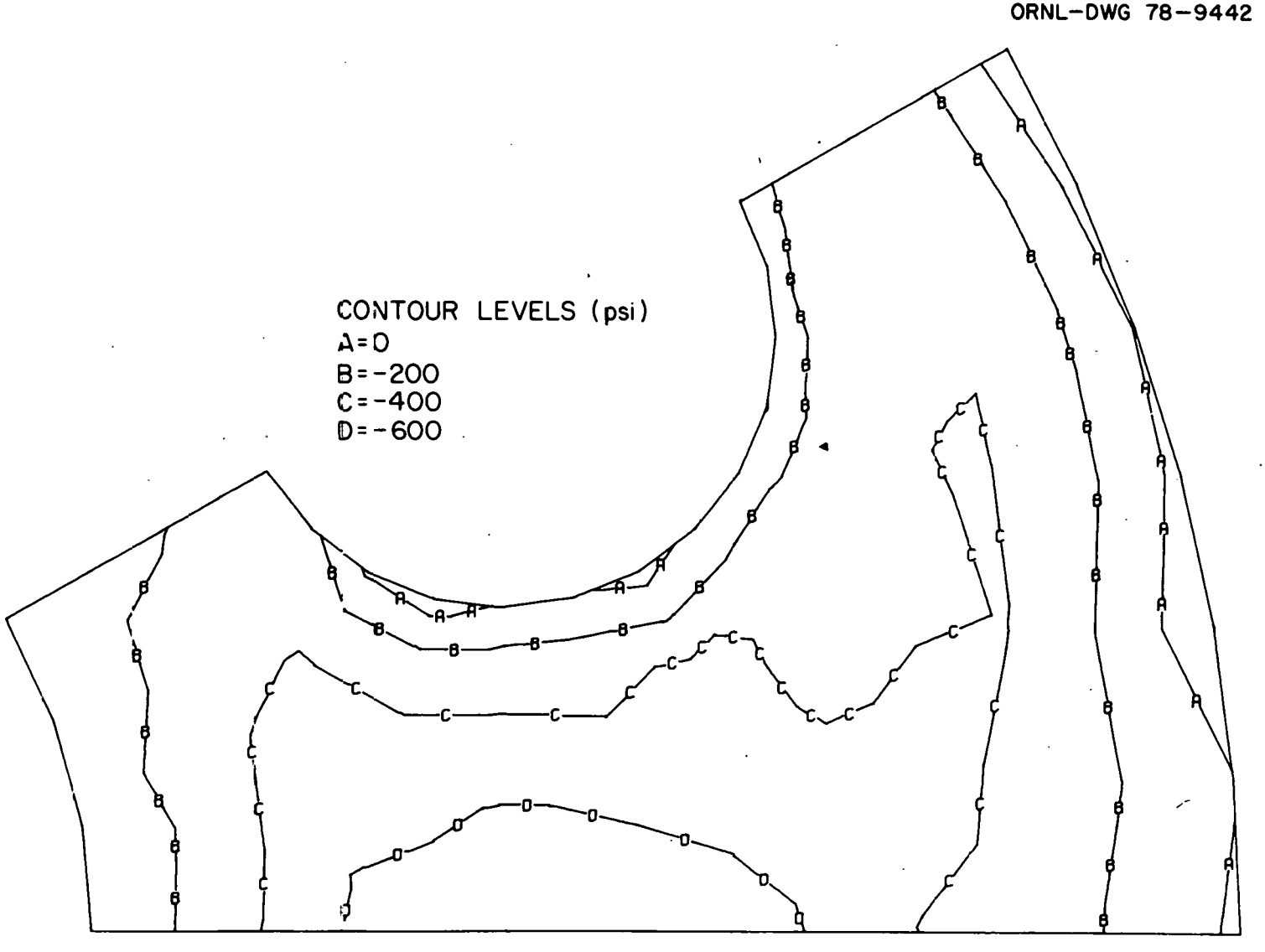

Fig. 34. Maximum principal stress at end of life due to temperature gradient for HTGR vessel.

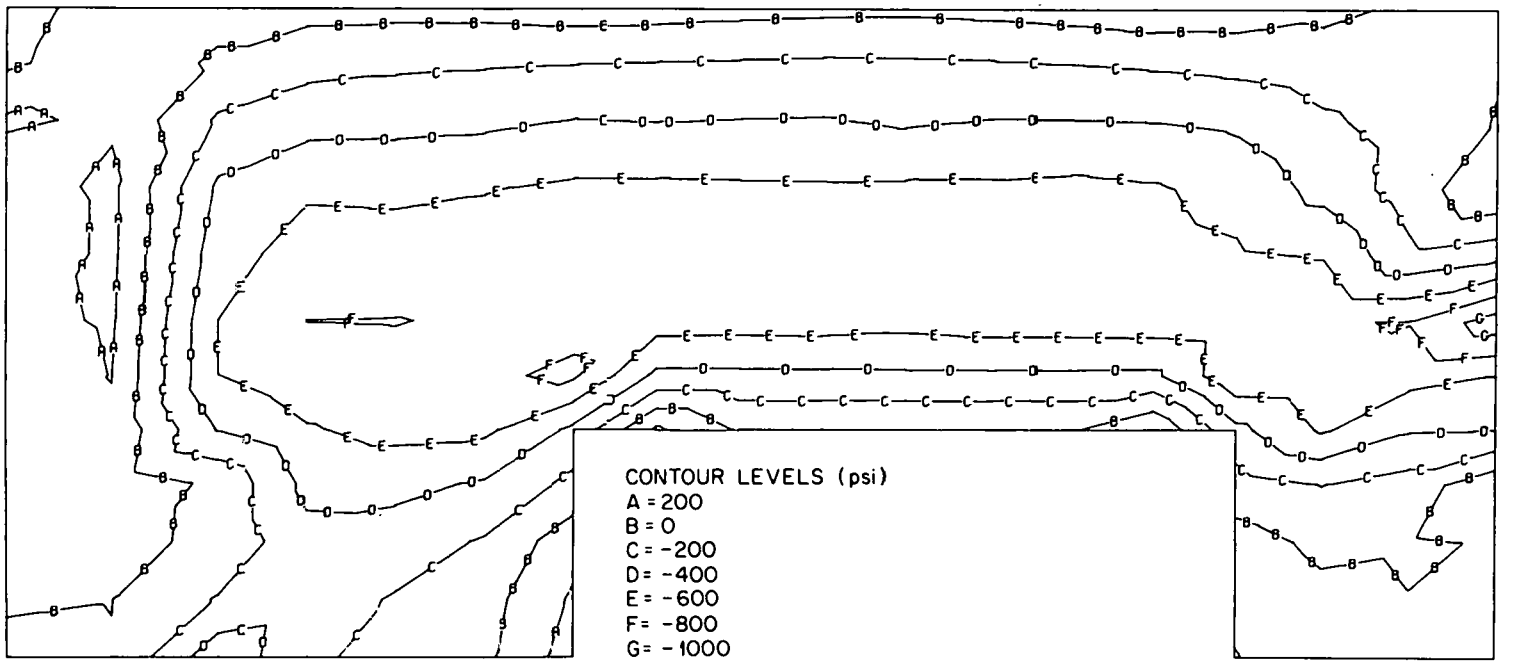

Fig. 35. Maximum principal stress at end of life due to temperature gradient for HTGR vessel.

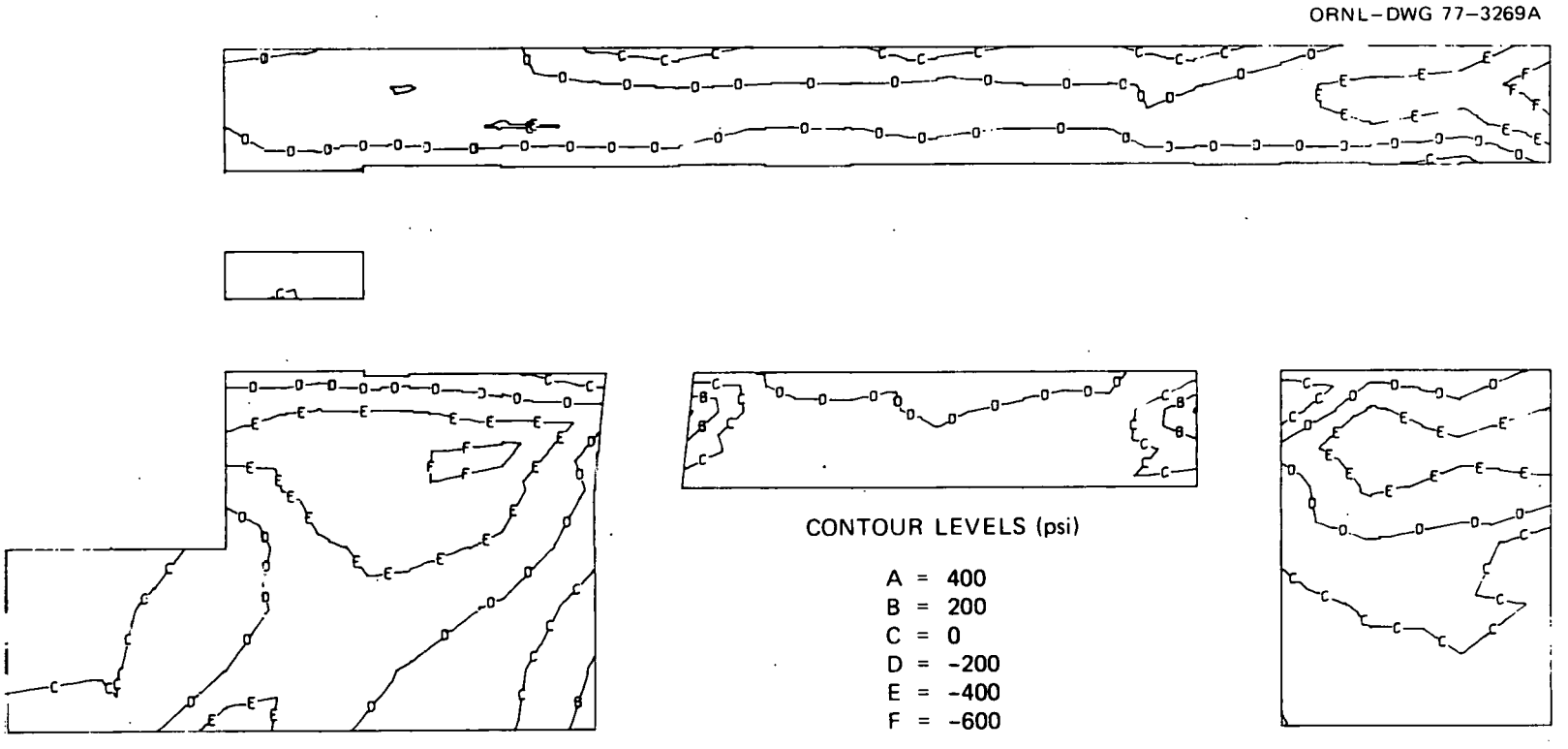

Fig. 36. Maximum principal stress at end of life due to temperature gradient for HTGR vessel.

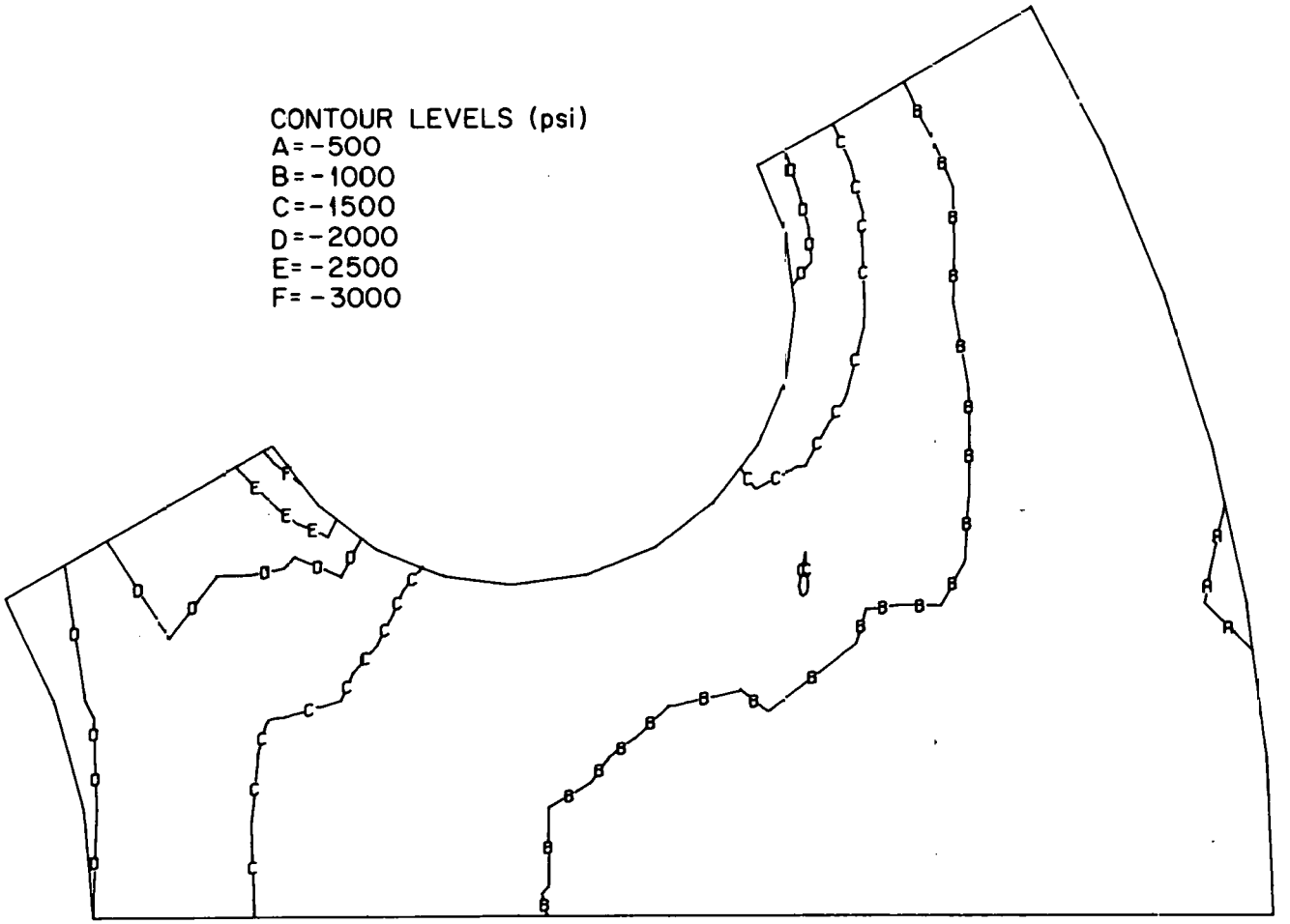

Fig. 37. Minimum principal stress at end of life due to temperature gradient for HTGR vessel.

ORNL-DWG 78-9450

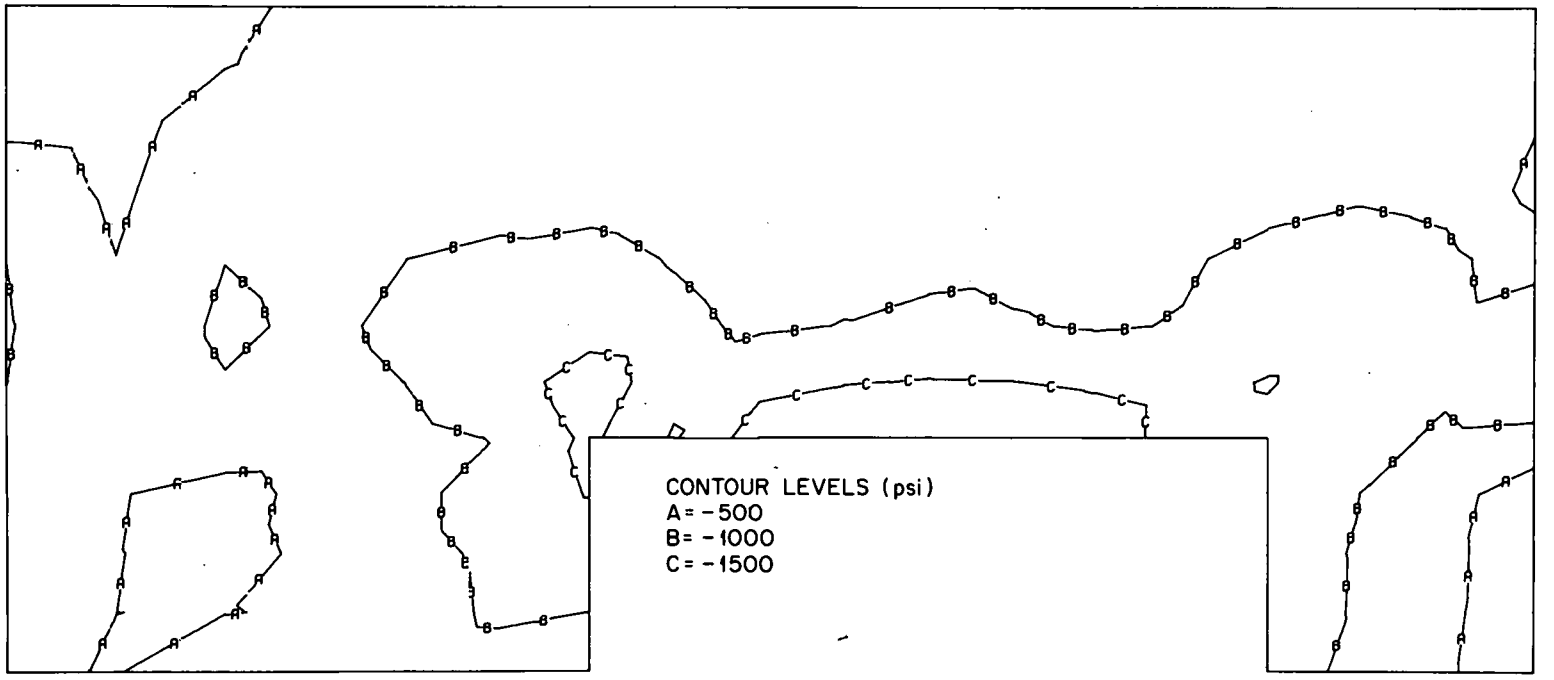

Fig. 38. Minimum principal stress at end of life due to temperature gradient for HTGR vessel.

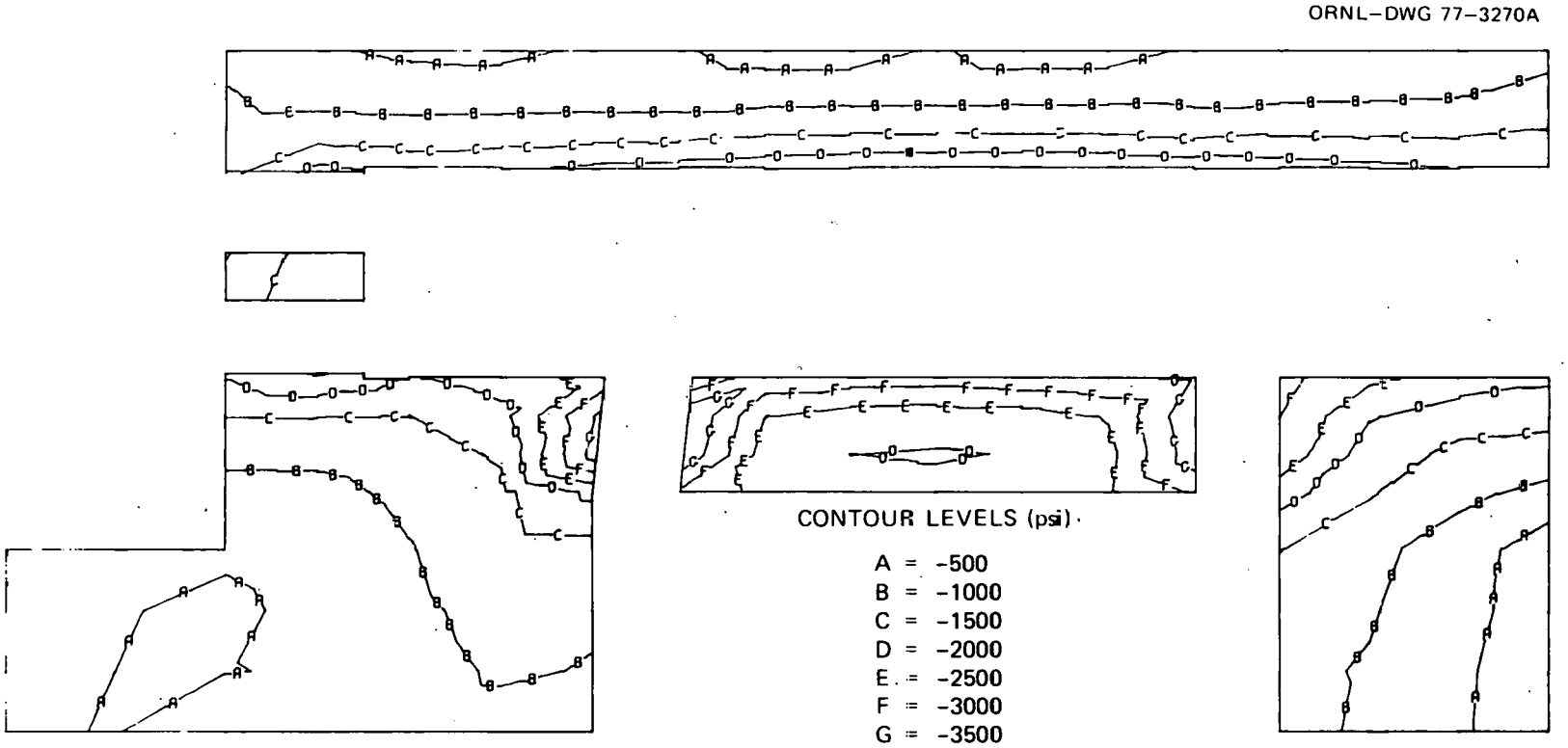

Fig. 39. Minimum principal stress at end of life due to temperature gradient for HTGR vessel.

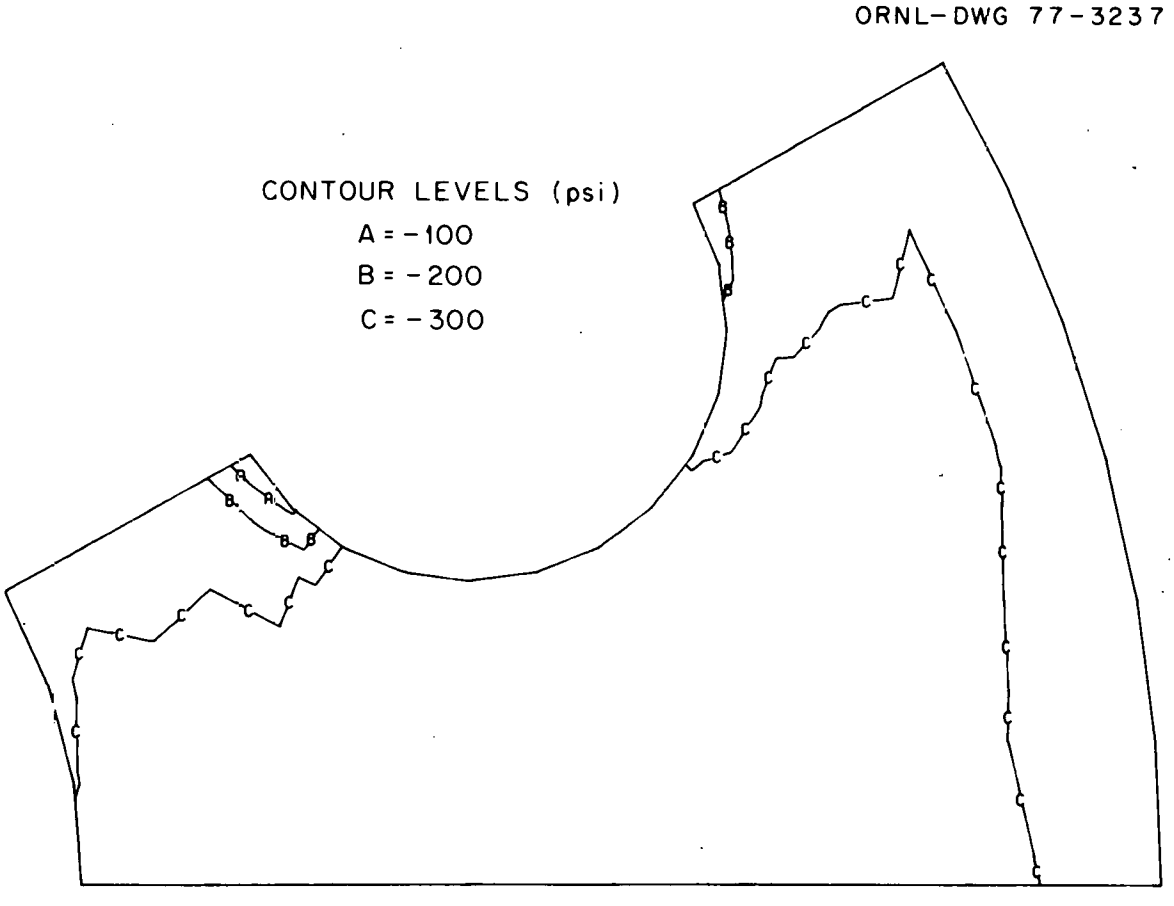

Fig. 40. Maximum principal stress at end of life due to maximum cavity pressure for HTGR vessel.

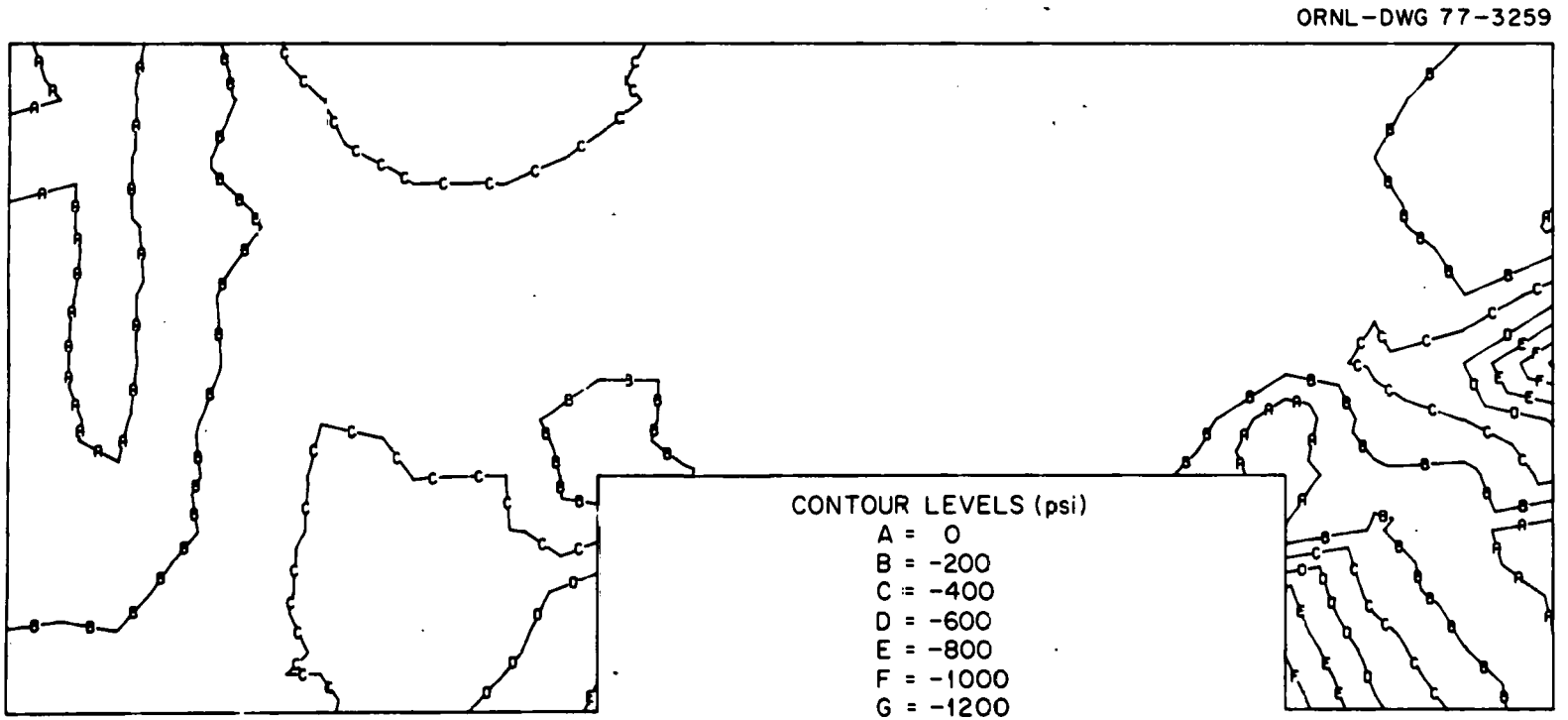

Fig. 41. Maximum principal stress at end of life due to maximum cavity pressure for HTGR vessel.

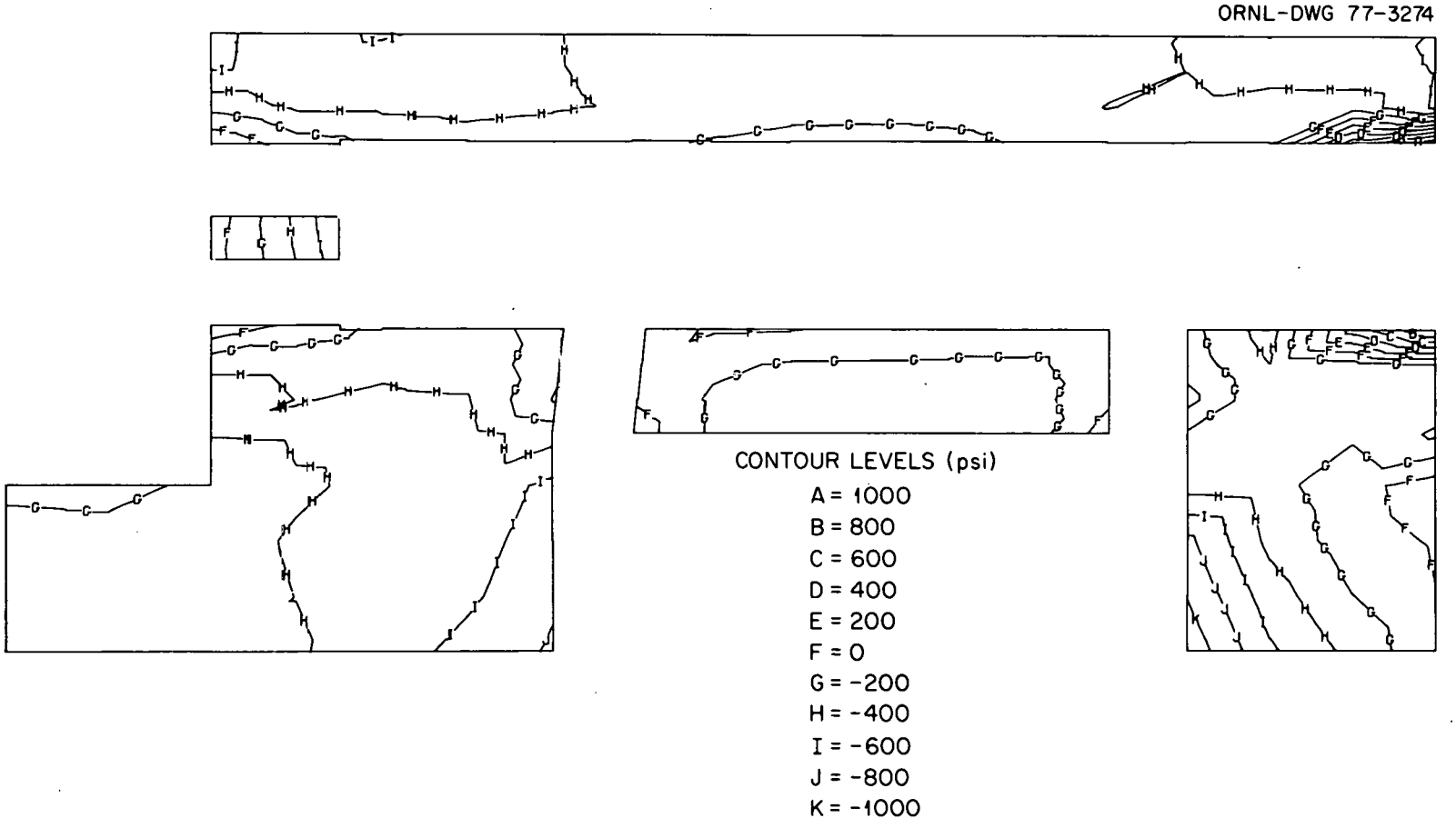

Fig. 42. Maximum principal stress at end of life due to maximum cavity pressure for HTGR vessel.

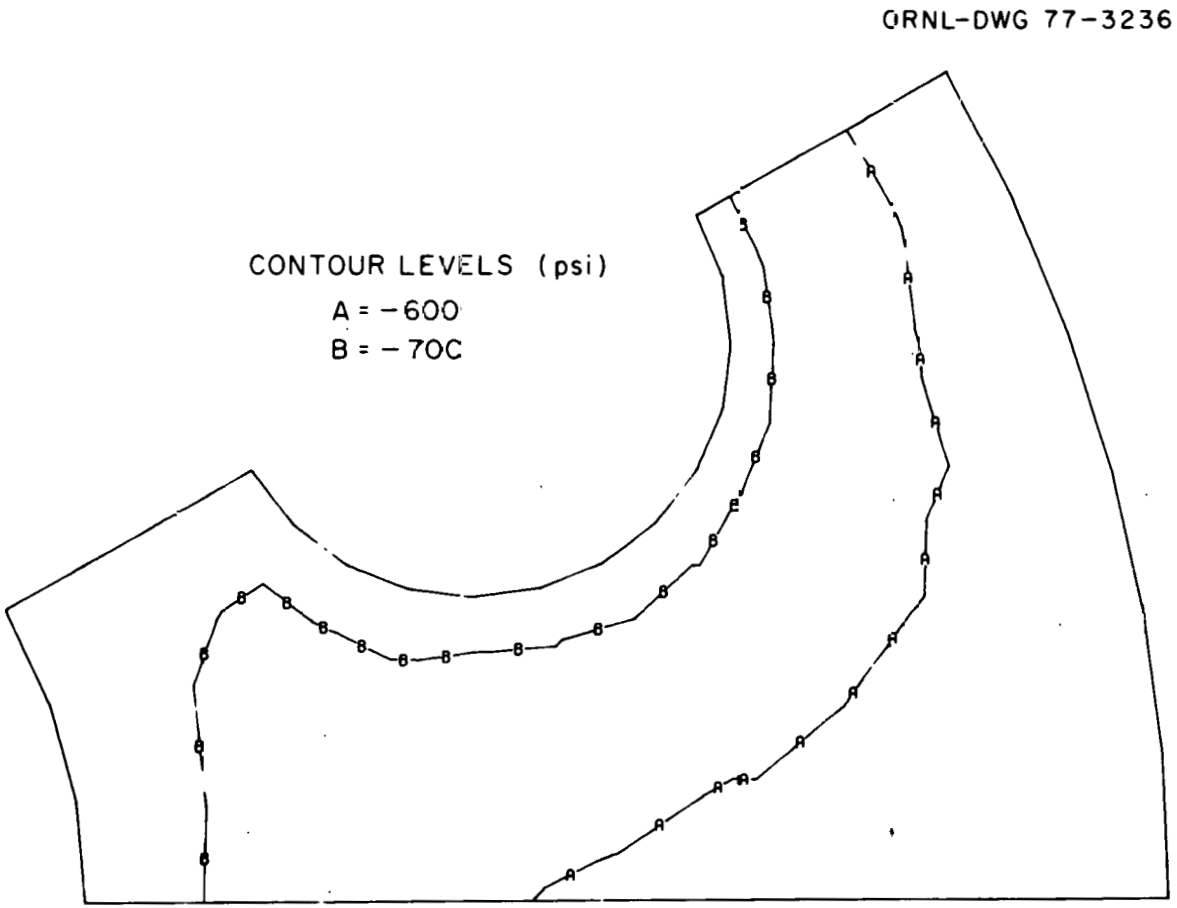

Fig. 43. Minimum principal stress at end of life due to maximum cavity pressure for HTGR vessel.

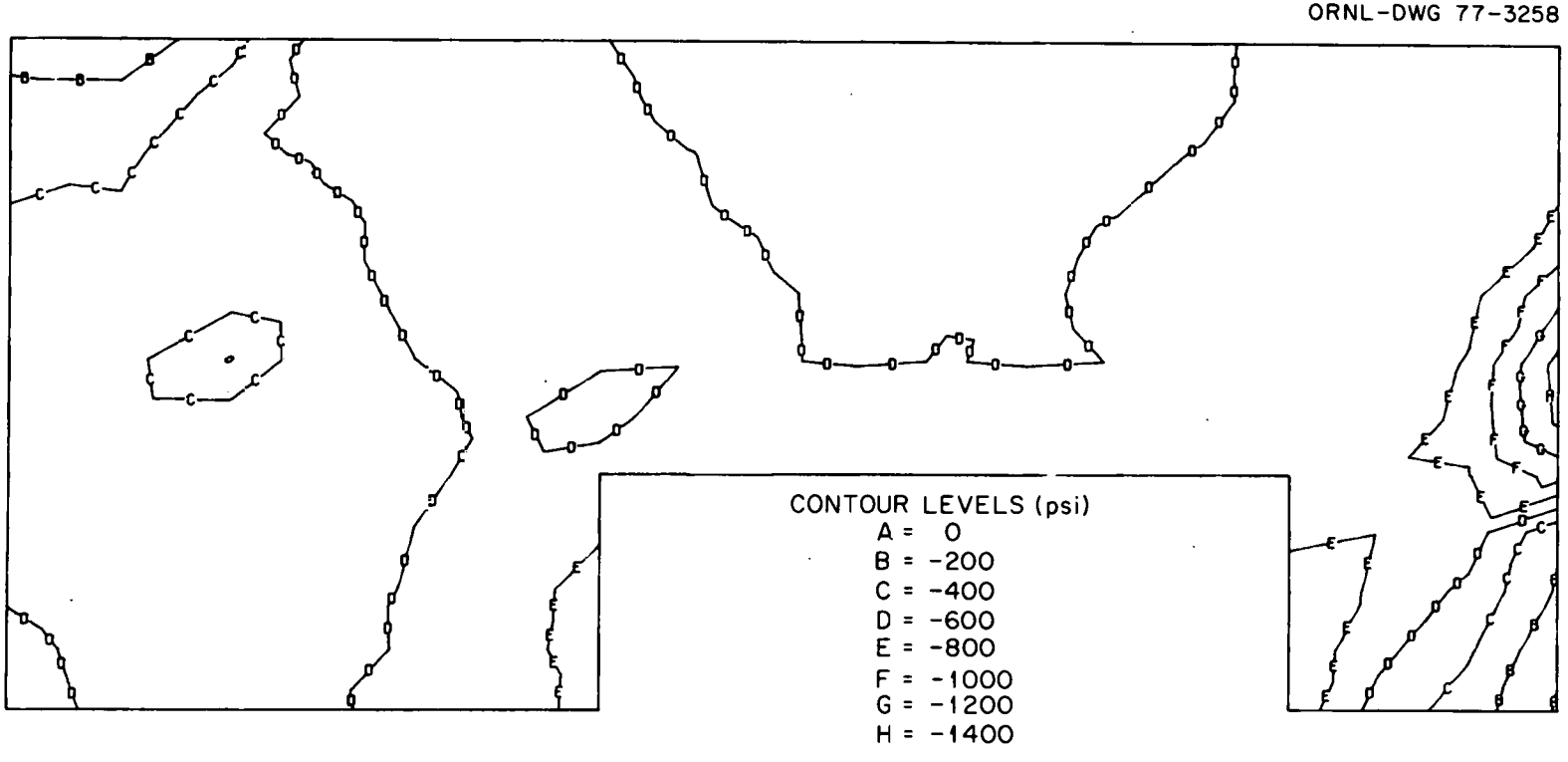

Fig. 44. Minimum principal stress at end of life due to maximum cavity pressure for HTGR vessel.

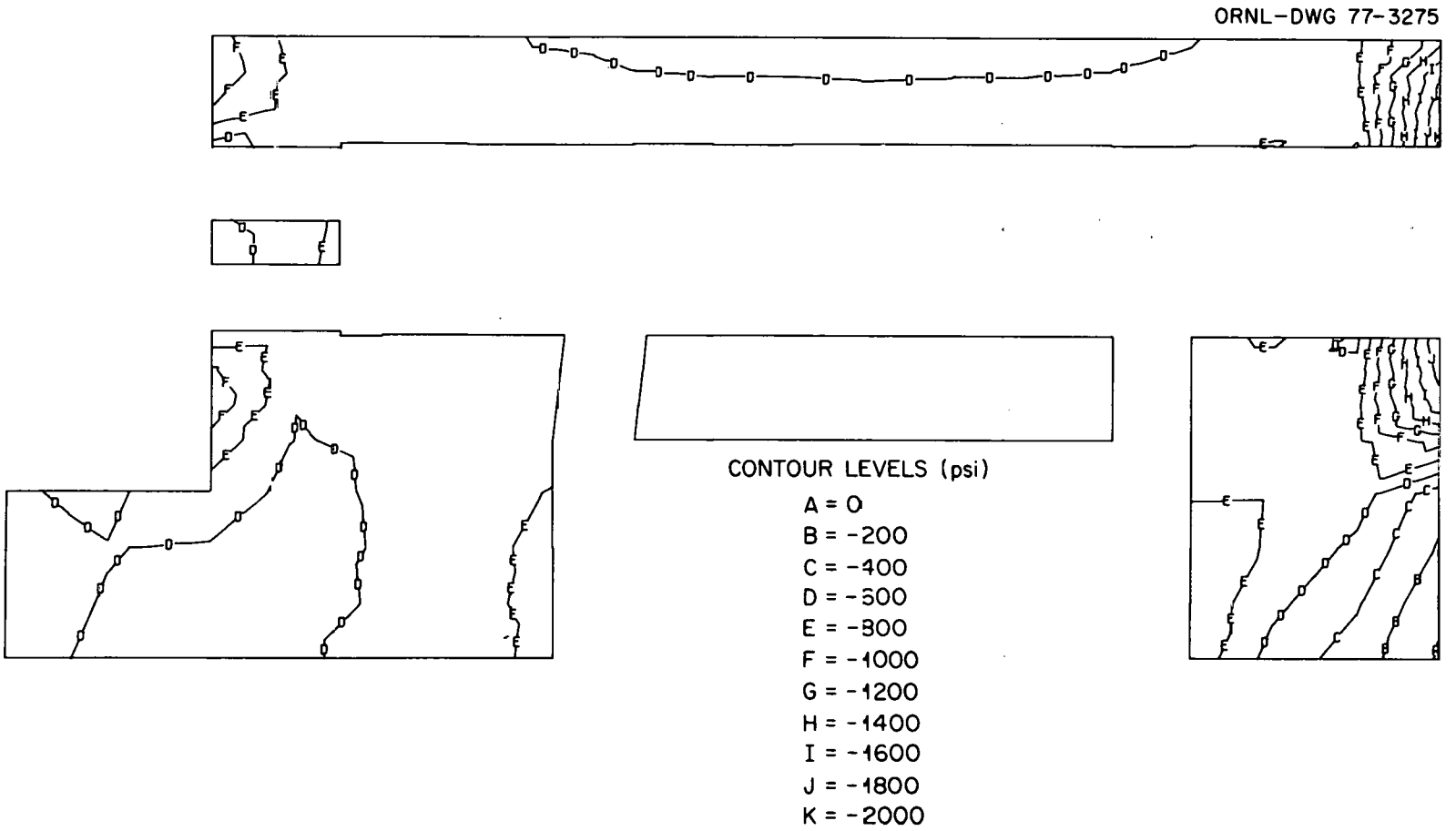

Fig. 45. Minimum principal stress at end of life due to maximum cavity pressure for HTGR vessel.

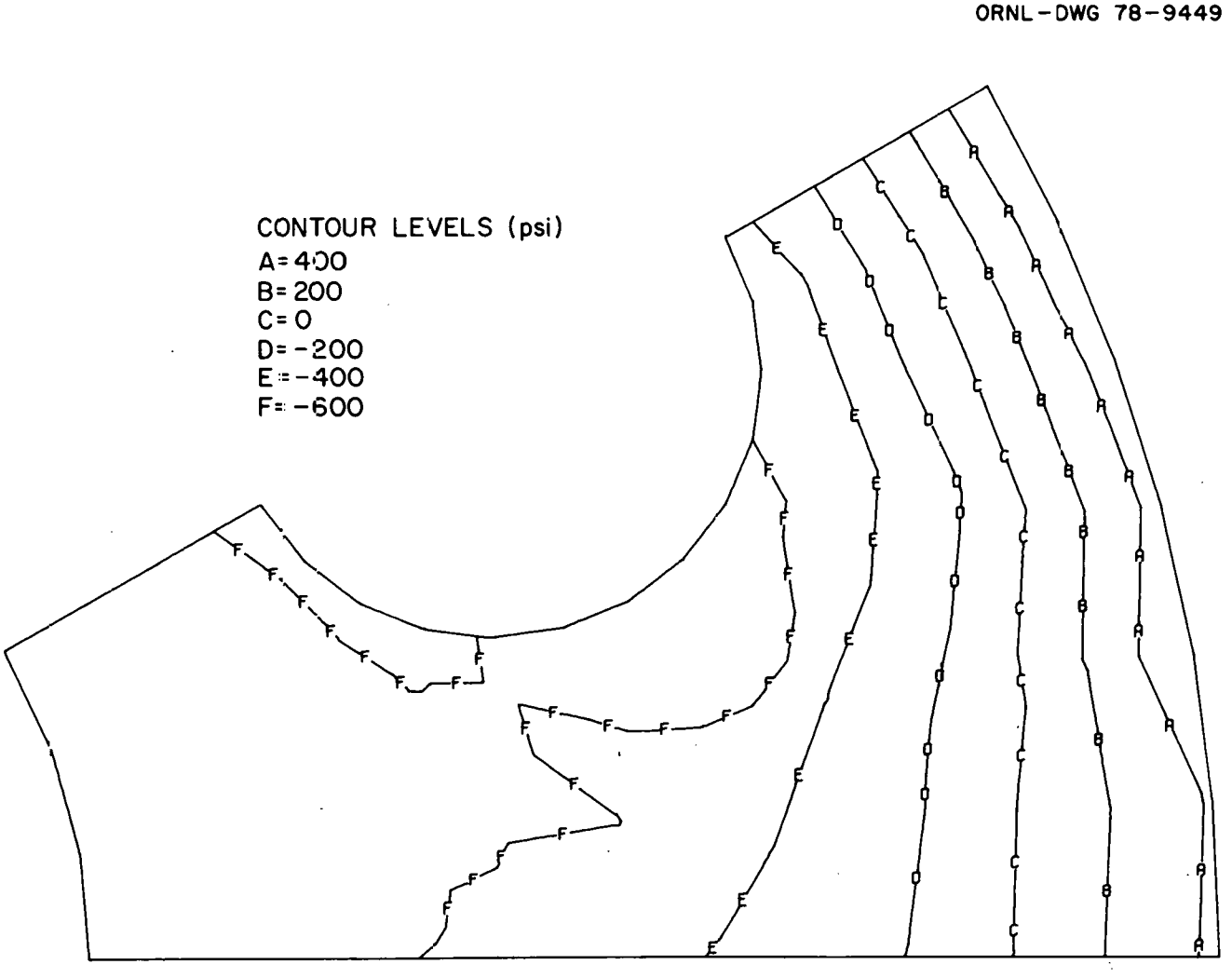

Fig. 46. Maximum principal stress at end of life due to temperature gradient and maximum cavity pressure for HTGR vessel.

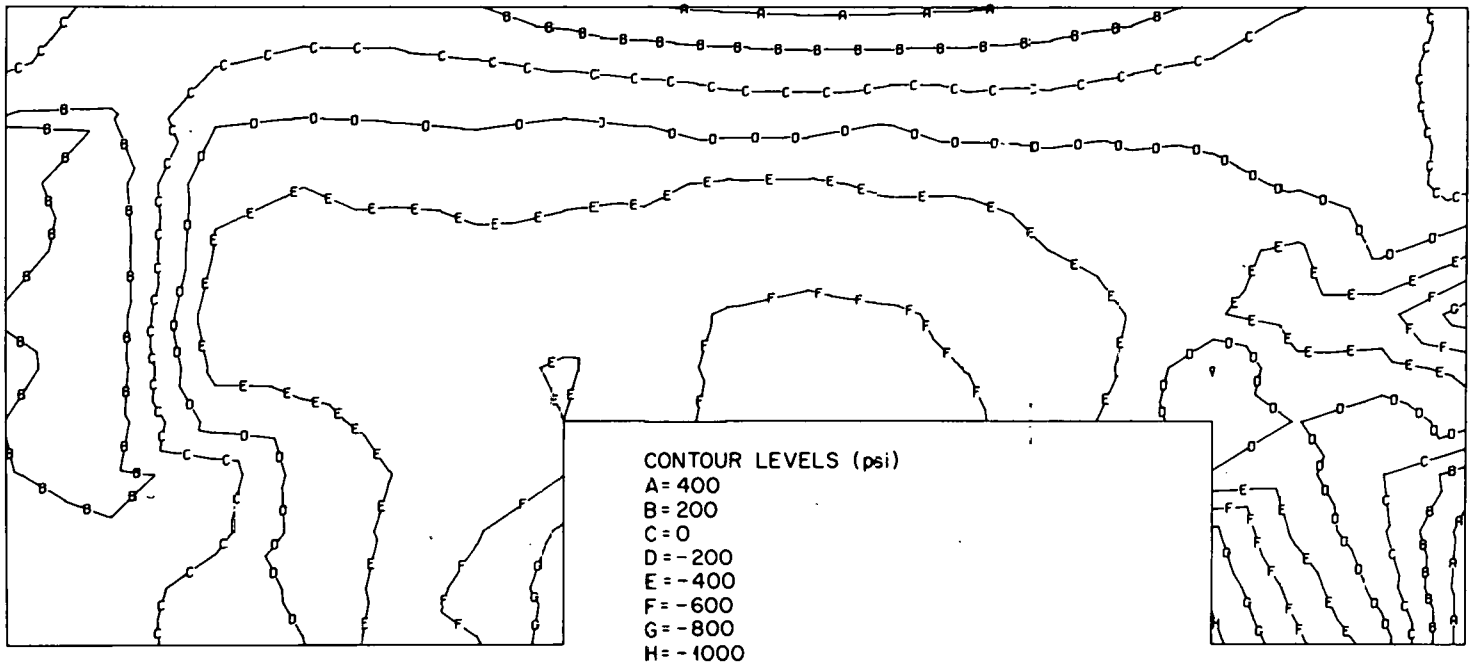

Fig. 47. Maximum principal stress at end of life due to temperature gradient and maximum cavity pressure fcr HTGR vessel.

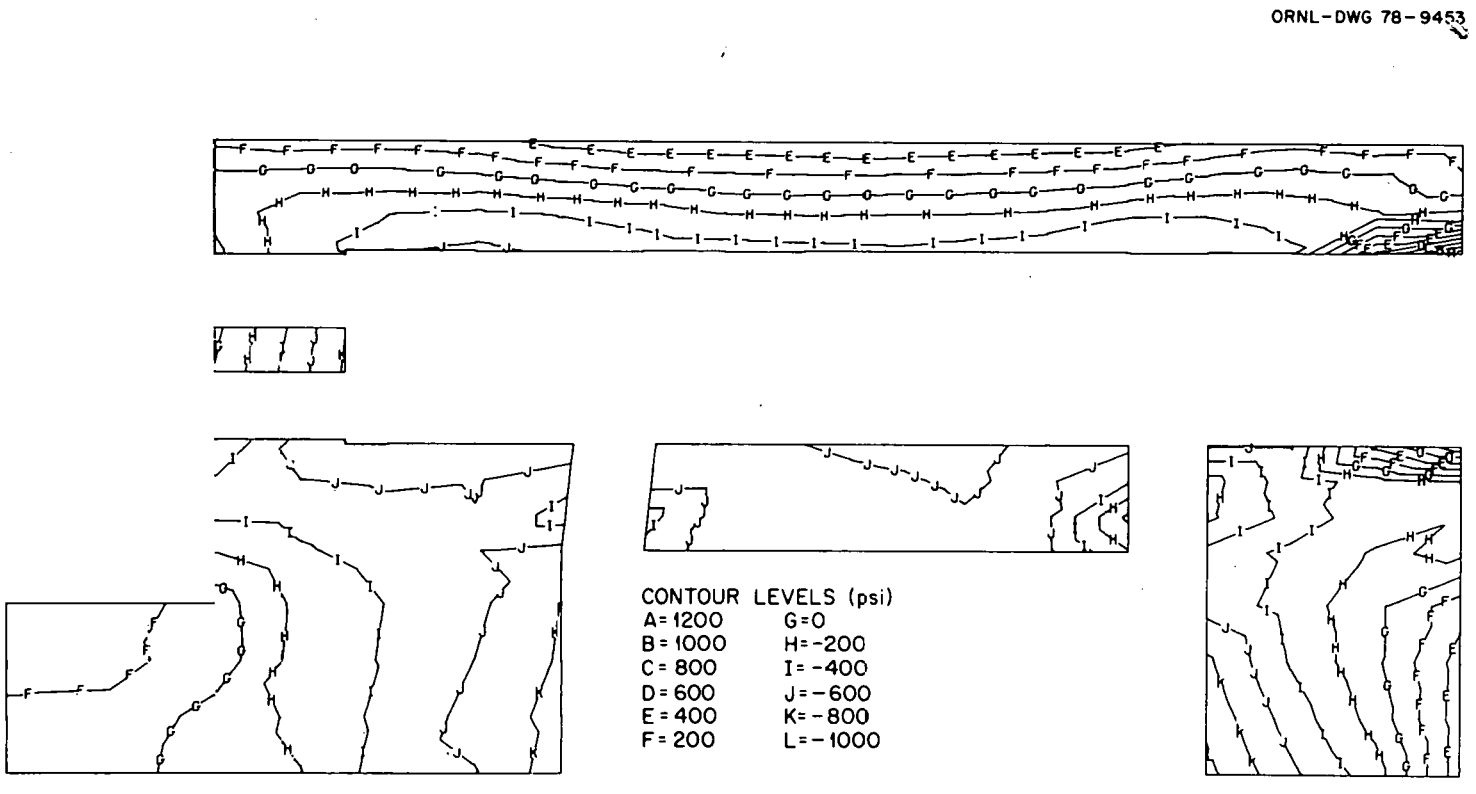

Fig. 48. Maximum principal stress at end of life due to temperature gradient and maximum cavity pressure for HTGR vessel.

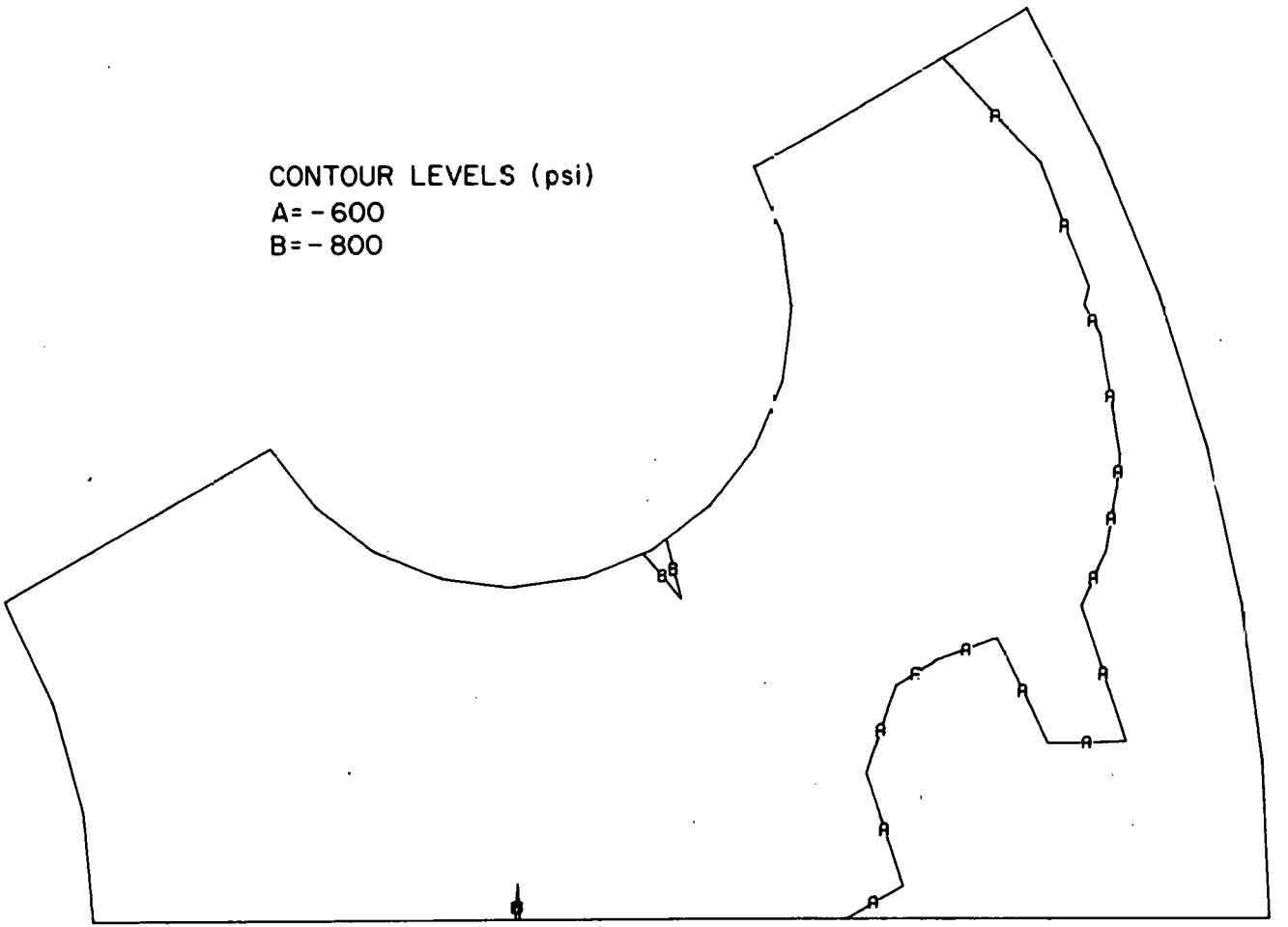

Fig. 49. Minimum principal stress at end of life due to temperature gradient and maximum cavity pressure for HTGR vessel.

ORNL-DWG 78-9446

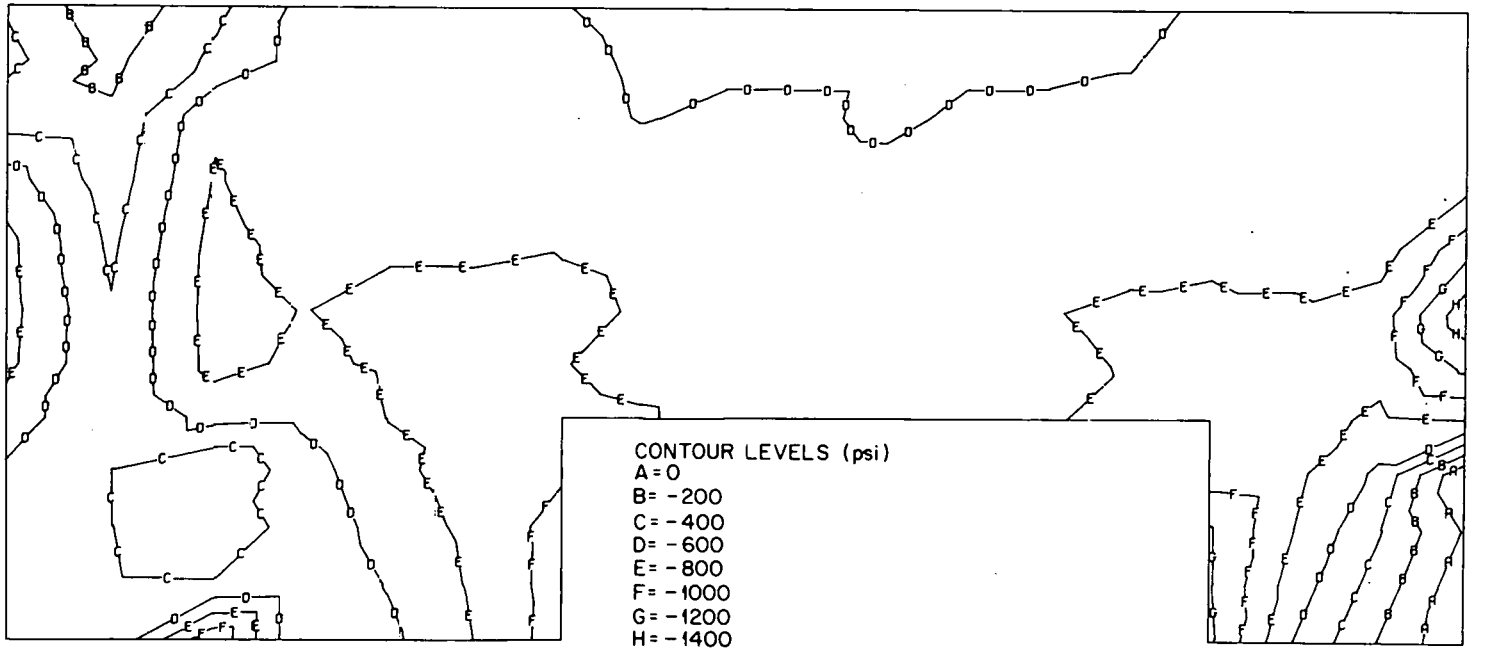

Fig. 50. Minimum principal stress at end of life due to temperature gradient and maximum cavity pressure for HTGR vessel.

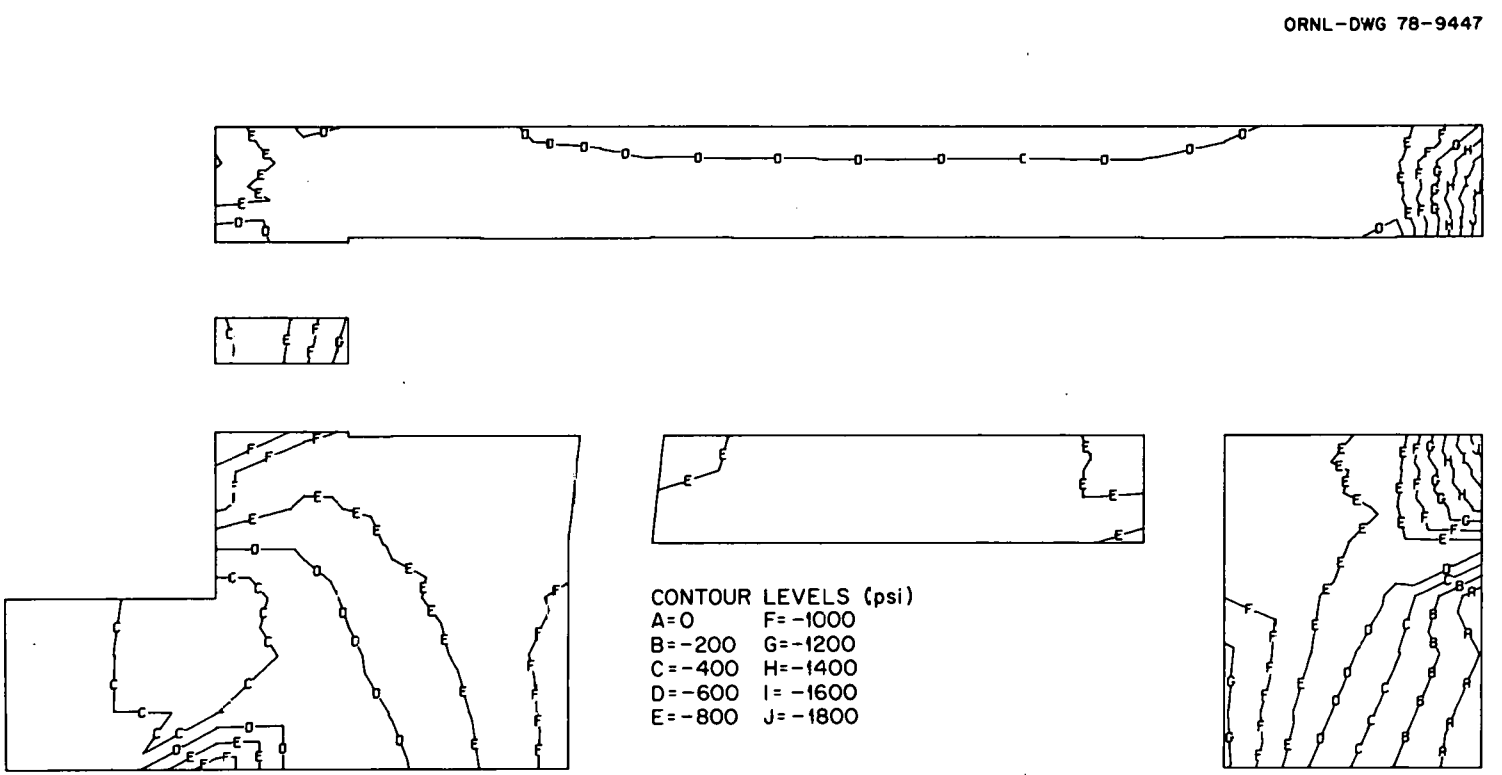

Fig. 51. Minimum principal stress at end of life due to temperature gradient and maximum cavity pressure for HTGR vessel.

REFERENCES

1. Finite Element Analysis of Mine Structures, Final Report to Denver Mining Research Center, U.S. Department of the Interior, Bureau of Mines, Contract H0110231 (September 1972).

2. T. Takeda et al., "Pressure Tests of PCRV Models," Seventh Congress of the Federation Internationale de la Precontrainte, New York, 1974.

3. Klaus-Jurgen Bathe, E. L. Wilson, and R. H. Iding, NONSAP: A Structural Analysis Program for Static and Dynamic Response of Nonlinear Systems, Report UC SESM 74-3, University of California, Berkeley (February 1974).

4. B. Saugy, Th. Zimmermann, and M. Hussain, "Three Dimensional Rupture Analysis of a Prestressed Concrete Pressure Vessel Including Creep Effects," Nucl. Eng. Des. 28, 97–120 (1974).

5. ASME Code for Reactor Vessels and Containments, Section III, Division 2, "Nuclear Power Plant Components," 1975.

THIS PAGE

WAS INTENTIONALLY

LEFT BLANK

ORNL/TM-6099
Dist. Category UC-77

Internal Distribution

1. S. J. Ball
2. D. E. Bartine
3. M. E. Bender
4-9. J. P. Callahan
10. D. A. Canonico
11. J. A. Clinard
12. J. A. Conlin
13. J. H. Coobs
14. W. E. Cooper
15. J. M. Corum
16. J. R. DiStefano
17. W. G. Dodge
18. J. R. Dougan
19. W. P. Eatherly
20. D. N. Fanning
21. Uri Gat
22. D. W. Goodpasture
23. A. G. Grindell
24. W. L. Greenstreet
25. R. C. Gwaltney
26. J. F. Harvey
27. F. J. Homan
28-36. P. R. Kasten
37. M. Levenson
38. A. L. Lotts
39. R. E. MacPherson
40. A. P. Malinauskas
41. W. J. McAfee
42. J. G. Merkle
43. R. K. Nanstad
44. D. J. Naus
45. K. J. Notz
46. C. B. Oland
47. G. C. Robinson
48. J. P. Sanders
49. M. R. Sheldon
50. G. M. Slaughter
51. G. C. Smith
52. J. E. Smith
53. H. E. Trammell
54. M. Tobias
55. D. B. Trauger
56. J. R. Weir, Jr.
57. G. D. Whitman
58. R. P. Wichner
59. G. T. Yahr
60. ORNL Patent Office
61-62. Central Research Library
63. Document Reference Section
64-67. Laboratory Records Department
68. Laboratory Records, ORNL-RC

Consultants and Subcontractors

69. E. G. Burdette, Civil Engineering Department, University of Tennessee, Knoxville, TN 37916
70. R. H. Gallagher, Civil Engineering Department, Cornell University, Ithaca, NY 14850

External Distribution

71-72. Director, Division of Nuclear Research and Applications, DOE, Washington, D.C. 20545
73. Director, Reactor Division, DOE, ORO
74-75. Director, Research and Technical Support Division, DOE, ORO
76-252. For distribution as shown in TID-4500 Distribution Category UC-77, Gas-Cooled Reactor Technology